Study of Collision Cross Section of Ultra-Cold Rubidium using a Magneto-Optic and pure Magnetic trap

by

David Fagnan

A THESIS SUBMITTED IN PARTIAL FULFILLMENT OF
THE REQUIREMENTS FOR THE DEGREE OF

BACHELOR OF SCIENCE

in

The Faculty of Science

(Combined Honours of Math and Physics)

THE UNIVERSITY OF BRITISH COLUMBIA

(Vancouver)

April 2009

Abstract

This thesis discusses a new technique for measuring collision cross sections, using a magneto-optical trap (MOT) or magnetic trap as well as theoretical predictions for the resulting measurements based on scattering theory. The initial discussion focuses on a theoretical overview of the principles involved in laser cooling and trapping, magnetic trapping, and scattering theory. Following this, a detailed overview of the experimental instruments and methods describing the vacuum system, laser light, magnetic coils, imaging and control systems will be presented. In addition to an experimental overview, the methods and mechanical formulation involved in predicting cross sections and loss rates based on scattering theory are discussed. Finally, an overview of both experimental and theoretical results including cross sections and loss rates for the case of trapped ^{87}Rb and background argon or helium gas will be given. The results gathered in this thesis show a strong dependence of elastic collision cross section on trap depth, which indicates that the majority of elastic collisions between ultra-cold rubidium and room temperature argon impart energy below 1K. These results suggest that the magnetic trap may be a better tool for measuring total elastic collision cross sections.

Table of Contents

List of Tables

List of Figures

Acknowledgements

My experience in the Quantum Degenerate Gas laboratory has been an engaging one and has given me the opportunity to apply my interest in physics from both an experimental and numerical point of view. I would like to thank both my supervisors, Dr. Kirk Madison, for his encouragment, engaging conversations and enthusiasm for his work, and Dr. James Booth, for his dedication, support in all areas of my research, and his sense of humour. Thank you also to Jicheng Wang and Dr. James Booth for helping me with many hours of data taking and analysis, without whom I would not have been able to complete my results. I would like to thank Dr. Bruce Klappauf for his participation in our discussions and insightful ideas and thoughts. I would also like to thank Janelle for her vast knowledge of the laser system and for being able to solve any associated problem I had.

I would also like to thank my friends and family who encouraged me to work hard and for their ever-present support in any endeavour I choose to undertake.

Chapter 1

Introduction

1.1 Overview

In the field of atomic molecular physics, laser cooling has become a central focus and an important tool. The Nobel Prize in Physics in 2001 was awarded to three physicists studying Bose-Einstein Condensates[1] (BECs) which were created using laser cooling and magnetic trapping. The experiment discussed in this thesis takes place in an ultra-high vacuum environment with background pressures that range from 10^{-9} to 10^{-7} Torr. We are primarily interested in trapping both ^{87}Rb and ^{85}Rb, the two naturally abundant isotopes of rubidium. Our measurements focus on loading rates and loss rates of trapped atoms in two specific neutral atom traps, the Magneto-Optical Trap(MOT) and the magnetic trap. Although the MOT captures from a room-temperature thermal distribution of natural rubidium atoms, the capture limit is a mere 1K, a small fraction of the peak of the Maxwell-Boltzmann distribution. In order to study trapped atoms in the magnetic trap, which has a capture limit around 1mK, we initially capture atoms in the MOT, and subsequently cool them further and transfer them into the magnetic trap.

Once we have atoms collected in either trap type we measure loading or loss rates which may be affected by trapping parameters, but mostly we care about the relationship of these rates on the background pressure. These room-temperature atoms undergo scattering with the trapped atoms which can lead to escape and loss of trapped atoms, this is key to our experiment. By measuring the loss rate at various background pressures we can extract a collisional cross section describing the size of the interaction between various pairs of atoms. The main result of our experiment which we will show is that while the Magneto-Optical trap and magnetic trap are both excellent tools for making benchmark measurements of cross sections, it is important to be aware of the effects of recapture. If a significant amount of collisions result in energy transfer which is too small to cause the trapped atoms to escape, then the measured cross section will be suppressed. These ideas will be detailed and discussed in the Theory section of this thesis.

1.2 Cross Section

The focus of this thesis is the measurement of total absolute elastic cross sections. The cross section is a hypothetical area that represents the likelihood of interaction between two particles. This thesis makes an experimental extraction of the cross section based on elastic loss rates in a trap, and compares this to calculations of the expected cross section from the principles of scattering theory. Throughout this thesis, cross section refers to the absolute elastic cross section, unless otherwise specified, and does not include inelastic losses.

1.3 Neutral Atom Traps

There are various neutral atom traps used in this work, including several variations and arrangements of magnetic traps, the MOT, and the optical dipole trap. Each has its own uses and relies on different methods for the trapping force. Overall though, laser cooling is a common theme and is required to slow atoms to within a trappable range of temperature for any given trap. Overall the trapping mechanism is quite fascinating, the neutral atom is essentially bombarded with photons that oppose its motion until its slow enough that it becomes stuck at the bottom of an energy well. Below, we discuss the details of the two traps used in this experiment and some typical values associated with them.

1.3.1 Magneto-Optical Trap (MOT)

The MOT has become the staple of cold atom physics, and is used for loading many of the other traps as it is very convenient for cooling atoms to temperatures below 1mK. It relies on laser cooling to capture from a thermal distribution of atoms at room temperature. Although the MOT makes use of a quadrupole pair in anti-Helmholtz configuration, the magnetic force is not used. Instead, the splitting caused by the generated magnetic field causes the resonance of light to become position dependant. MOTs have the capability of capturing up to 10^9 atoms [13]. Although this is small fraction of the distribution, it is sufficient to perform a wide variety of cold atom experiments. For our MOT, we estimate trap numbers to be in the range of 10^5-10^7 depending on the alignment and various conditions. For these reasons the MOT is a very useful tool in preparing and even studying confined atoms at low temperatures. They have been studied thoroughly over the past few decades

Unfortunately, the near resonance lasers continue to barrage the trapped atoms while they sit trapped in the MOT. This leads to what has been named the recoil limit, caused by spontaneous emission momentum kicks. For the case of rubidium, this recoil limit is on the order of a few hundred μK [12]. This recoil limit causes problems when trying to work towards a BEC, preventing arbitrary low levels of cooling and the required phase space density to cause the relevant transition. This is one reason why the MOT is often used to load another neutral atom trap. However, in our experiment we are not interested in the creation of a BEC, the reason for interest in traps other than the MOT comes from the large trap depth it maintains. The magnetic trap we use has a trap depth roughly 3 orders of magnitude smaller, and is hence able to reduce the chance of recapture. In particular, we will compare the differences between the two trap types and attempt to predict them from traditional scattering theory.

1.3.2 Magnetic Trap

There have been a wide variety of magnetic traps used in cold atom physics ranging from the simple quadrupole pair, the QUIC trap, as well as some more involved traps such as the TOP trap. All these magnetic traps affect the atom via the magnetic moment of the atoms which interacts with an inhomogeneous magnetic field. We employ the same coils used in the MOT, the quadrupole pair in anti-Helmholtz configuration. Unlike the MOT, here we increase the current in the coils so that a gradient to oppose gravity is generated. When atoms are loaded to the MOT, by turning off the lasers and ramping the coil current, they become held against gravity. Typically, with appropriate cooling and alignment, we can achieve capture from the trapped atoms in the MOT between $40-50\%$. In the case of ^{87}Rb and ^{85}Rb, only about half the magnetic hyperfine levels are actually trappable, the other hyperfine levels will be accelerated by the magnetic field and by gravity. Without appropriate spin-pumping on these transitions, the $40-50\%$ capture fraction currently achieved is excellent.

Although the magnetic trap is limited in trap depth, it is a good choice for our experiment because we want to study collisions in the limit of zero trap depth. The reason for this will be discussed in detail in this thesis and the magnitude of its importance is quite astonishing. As we are interested in studying collisions caused by the room-temperature background atoms, the magnetic trap has the advantage over the MOT that this is the only collisions that occur. In the MOT, there are light-induced collisions which make the study of atom dynamics unnecessarily

complicated. Although using the quadrupole pair in anti-Helmholtz configuration is convenient, it does introduce the problem of Majorana spin-flip losses. This is caused when atoms of sufficiently high temperatures experience a quickly changing magnetic field. The effects of these Majorana losses will be further discussed in the theory section of this thesis.

1.4 Applications

Taking a step back for a moment, I will discuss some of the recent applications of this field, as well as possible future applications that are currently being developed. Recently the development of an atom chip[2], an integrated device used to confine, control, and manipulate atoms, allows for the possibility of portable devices based on laser cooled atoms and Magneto-Optical Traps (MOT). Currently research[3] is already underway exploring the possibility of a quantum gate with such atom chips. The MOT that we have used in our experiment is a significantly smaller MOT and plans in our lab to further scale down the size of the MOT with the use of an atom chip are already underway.

In order to work towards eventualities such as the quantum gate and atom chip based devices, it is important to understand the loss mechanisms of the magnetic traps used to create BECs[1][8]. A practical limit to the magnetic trap lifetime is imposed by the presence of residual gas in ultra-high vacuum systems[9]. In order to create portable devices based on this technology, it is important to be able to maintain high lifetimes, and hence we need to learn more about the dominant losses involved[10].

Chapter 2

Theory

This chapter is meant to prepare the reader for the concepts that are involved in this experiment as well as a detailed description of the relevant equations and approximations used to model the experiment.

2.1 Starting Equations

Although some of the theory that will be presented has been detailed elsewhere, rather than simply present the relevant equations, I will attempt to present the origin of equations and the necessary approximations required to validate them. We begin with the well known time-dependent Schrodinger equation,

$$\mathrm{H}\Psi(\vec{r},t) = i\hbar\frac{\partial\Psi(\vec{r},t)}{\partial t}, \tag{2.1}$$

where H is the total time dependent Hamiltonian, r is the position of the electron, and Ψ is the wave function. We then separate the total Hamiltonian into a time-dependent part, $\tilde{\mathrm{H}}$, and its time-independent part, $\mathrm{H_o}$. We can then work in the basis of eigenfunctions resulting from the time-independent problem,

$$\Psi(\vec{r},t) = \sum_k c_k(t)\phi_k(\vec{r})e^{-i\omega_k t}, \tag{2.2}$$

since the basis functions Ψ_n form a complete set. The eigenvalues given by the resulting equations for each basis function, $\mathrm{H_o}\Psi_n = \mathrm{E_n}\Psi_n$. The $c_k(t)$ are arbitrary functions of time that satisfy the problem for the given time-dependent Hamiltonian. Substituting this expansion into the Eq. 2.1, multiplying on the left by ϕ_j^* and integrating over the spatial domain results in a system of ordinary differential equations for the basis coefficients. Writing $< \phi_j^*|\tilde{\mathrm{H}}_\mathrm{jk}|\phi_k >$ as $\tilde{\mathrm{H}}_\mathrm{jk}$ they are,

$$i\hbar\frac{dc_j(t)}{dt} = \sum_k c_k(t)\tilde{\mathrm{H}}_\mathrm{jk}(t)e^{i(\omega_j-\omega_k)t}. \tag{2.3}$$

These equations are the typical equations used in perturbation theory, discussed in typical text-books [23], however at this point they are still an exact representation of the Schrodinger equation.

2.2 Scattering Rate

This groundwork allows us to define the density matrix, where the matrix elements are given by

$$\rho_{ij} =< \phi_i|\rho|\phi_j >= c_i c_j^* \tag{2.4}$$

with the definition of basis functions presented. Using this definition with Eq. 2.1 we derive the time dependence equation for the density matrix,

$$i\hbar\frac{d\rho}{dt} = [\mathrm{H}, \rho]. \tag{2.5}$$

From this point, we can make the approximation that the atom has only two states, a ground state and an excited state which are connected by an appropriate laser frequency. The two-level model is a valid approximation when the laser detuning is significantly less than the two-level transition frequency. In practice, we can verify this assumption by checking that the probability of other transitions is insignificant. This allows us to write the density matrix as a 2x2 matrix, where the elements are given by Eq. 2.4 and obey Eq. 2.5. Then by separating the effects of the coupling to the external (light) field and quantum field (spontaneous decay) we can determine the full equations of motion for each of the four matrix elements. The assumption that these effects are independent holds when $\Omega \ll \omega_o$, where Ω is the Rabi frequency.[12].

To calculate the first effect, caused by coupling to the external field, we will provide an overview of only the effects of the light field on the atom. We impose two approximations on the general Hamiltonian, namely, the Rotating-Wave Approximation (RWA) and the electric dipole approximation. The RWA approximation is that the laser frequency must be near the resonant frequency of the two states, or $\delta \ll \omega_l + \omega_o$. This essentially results in ignoring terms in the Hamiltonian which oscillate with frequencies $\omega_l + \omega_o$, and keeping only those that oscillate with frequency $\omega_l - \omega_o$ [23]. The electric dipole approximation, another well known approximation in the field, ignores the spatial effects of the electric field. We can then write the electric field as a simple plane wave traveling in the z-direction which is given by,

$$\vec{\mathcal{E}}(\vec{r}, t) = E_o\hat{\varepsilon}\cos(kz - \omega_l t), \tag{2.6}$$

where $\vec{\mathcal{E}}$ is the electric field, E_o is the amplitude of the wave, and $\hat{\varepsilon}$ is the unit polarization vector. The corresponding Hamiltonian is derived in Metcalf's book,

$$\tilde{\mathrm{H}}(t) = -e\vec{\mathcal{E}}(\vec{r}, t)\cdot\vec{r} \tag{2.7}$$

where e is the electric charge. Now that we have the time-dependant equations for c_k, which in the two-level system result in a pair of coupled Ordinary Differential Equations (ODEs) as described in Eq. 2.3, we can find the element $\tilde{\mathrm{H}}_{12}$. This element is given by,

$$\tilde{\mathrm{H}}_{12}(t) = \hbar\Omega\cos(kz - \omega_l t), \tag{2.8}$$

where $< 1|$ and $< 2|$ are the ground and excited state eigenfunctions respectively, and Ω is the well known Rabi frequency defined by

$$\Omega \equiv \frac{-eE_o}{\hbar} < 1|r|2 > \tag{2.9}$$

Using a standard trick to uncouple the two coupled equations, the result is (after the RWA),

$$\frac{d^2c_1(t)}{dt^2} - i\delta\frac{dc_1(t)}{dt} + \frac{\Omega^2}{4}c_1(t) = 0 \tag{2.10}$$

and

$$\frac{d^2c_2(t)}{dt^2} + i\delta\frac{dc_2(t)}{dt} + \frac{\Omega^2}{4}c_2(t) = 0 \tag{2.11}$$

which we can quickly apply to the time dependant equation for the density matrix elements.

We then need to consider the second effect, known as spontaneous emission. This is significantly easier to work with as we can model the process as a simple exponential decay from the excited state to the ground state. This has been derived, by Einstein, who simply used detailed balancing of the two processes in a stochastic processes approach, but also by theory based on fluctuations of the quantized vacuum field[12]. Combining this exponential model with the effects caused by coupling to the external (light) field, we arrive at the well known optical Bloch equations (OBE).

In the steady state, we get the solution for the density element associated with the excited state which can be written as,

$$\rho_{ee} = \frac{s_o/2}{1 + s_o + (2\delta/\gamma)^2} \tag{2.12}$$

where s_o is known as the saturation parameter, defined by the ratio I/I_s. Where I_s is the saturation intensity, which is unique for each atom, given by

$$I_s \equiv \frac{\pi\hbar c}{3\lambda^3\tau} \tag{2.13}$$

where γ is the decay rate of the excited state due to spontaneous emission, and λ is the debroglie wavelength. Finally with the steady state solution in hand, we can determine the total scattering

rate of atoms by setting the decay rate of the excited state equal to the excitation rate of the ground state. This results in

$$R = \frac{\gamma}{2}\frac{s_o}{1 + s_o + (2\delta/\gamma)^2} \tag{2.14}$$

where R is the scattering rate in *photons/atom/sec*. The use of knowing this scattering rate is that we can measure the amount of light coming off the excited state atoms by use of a detector, and thus infer the physical number of trapped atoms. It should be noted here that we ignore the effects of scattered light on the atoms itself, assuming all light travels radially outwards in a uniform manner.

2.3 Trapping and Cooling Forces

2.3.1 1-D Molasses

Now that we have the scattering rate due to light for an atom, we can devise a trap for a neutral atom in its ground state. Laser cooling forces are caused by the momentum transfer from photons which are scattered by the atom. The two-level atom in the ground state absorbs the photon and enters the excited state, with the corresponding momentum transfer discussed above. Spontaneous emission can then cause the atom to drop back down to another ground state, this causes a momentum recoil as well, but since this is equally likely in all directions, they should average to zero over many scattering events[15][12]. As a result the net force on the atom is in the direction of the incoming photons that it can absorb. This force should be given by the momentum from each photon*the number of photons absorbed per second, mathematically,

$$\vec{F} = \hbar\vec{k}R \tag{2.15}$$

where $\vec{k}$ is the wavevector of the light and R is the scattering rate from Eq. 2.14. In the 1-D case, we can setup two counter-propogating red-detuned lasers. With the resulting equations presented so far, the forces would be equal and hence not change the atom's course. However, we have forgotten an important factor here, namely, the Doppler effect. Much as the typical application to sound frequencies, here we will see a shift in detuning frequency due to the velocity of the atom. The Doppler shift has a simple effect on detuning, creating what we will call effective detuning,

$$\delta_{\text{eff}} = \delta - kv \tag{2.16}$$

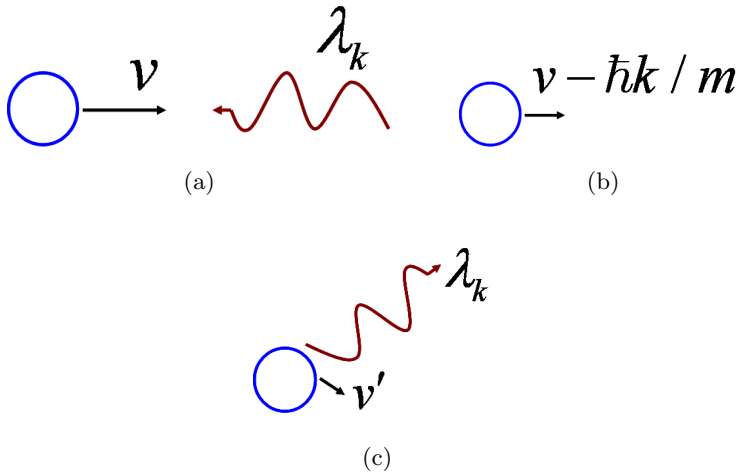

Figure 2.1: Depiction of light interactions of trapped particles to an on-resonant laser. a) An incoming photon of wavelength λ_k=$2\pi/k$, where k is the wavevector of the light, opposes the direction of motion of a particle with speed v. b) The photon has been absorbed and the speed of the particle has been reduced by the corresponding momentum transfer of the photon. c) Shortly after the absorption event, the excited state atom undergoes spontaneous emission in which it emits a photon of wavelength λ_k in a random direction.

where v is the velocity of the atom. This causes the beam opposing the motion of the atom to have a much higher scattering rate than the beam opposite (which gets an increase in effective detuning). This causes the atom to scatter more photons from the direction opposing its motion, causing it to slow to a speed predicted by the momentum kick of spontaneous emission. You can now think of this setup in 1-D as a molasses, there is no position dependant force, so the atom will undergo a random walk eventually leading outside of the beams and hence escaping the trap. By improving beam size and optical setup, you can delay the atom's escape as if the atom was travelling through a thicker medium. The magnitude of the force from one laser is therefore given by,

$$F_{\pm} = \pm\hbar k \frac{\gamma}{2} \frac{s_o}{1 + s_o + (2(\delta \mp kv)/\gamma)^2}, \tag{2.17}$$

and the combined force from the two lasers is, to lowest order Taylor expansion in kv/δ,

$$F = 8\hbar k \frac{s_o(\delta/\gamma)kv}{(1 + s_o + (2\delta/\gamma)^2)^2}. \tag{2.18}$$

It is important to notice here that this force is not position dependant, and is only in effect if the atom is within the beam size of the lasers.

2.3.2 Magneto-Optical Trap and the Zeeman effect

The Magneto-Optical trap is created using the laser cooling forces described with the help of a magnetic field[12][13]. The only thing missing from the optical molasses described is a position dependence in the overall force, something which keeps the atom within the area of beam overlap. In the MOT, this can be created by a variety of magnetic field setups, but in our case we use the traditional anti-Helmholtz coil setup. This results in a linear magnetic field gradient near the centre of the trap which causes shifts in the energy levels of

$$\Delta E = -\mu_{\mathrm{B}} g_{\mathrm{F}} m_{\mathrm{F}} \frac{dB}{dz} z \tag{2.19}$$

where $\frac{dB}{dz}$ is the magnetic field gradient, g_{F} is the Lande g-factor of the state, m_{F} is the magnetic spin of the state and z is the distance from the centre of the magnetic trap. Since the atomic resonance relies on the difference in energy between the ground and excited state this results in an effective detuning of

$$\delta_{\mathrm{eff}} = \delta - kv + (g_{\mathrm{F}'} m_{\mathrm{F}'} - g_{\mathrm{F}} m_{\mathrm{F}}) \mu_B \frac{dB}{dz} z/\hbar \tag{2.20}$$

where the $'$ notation refers to the excited state. This causes the position dependant radiation pressure force required to create the magneto-optical trap (MOT) as depicted in FIG. 2.2. For a simple two-level system, we use σ^+ and σ^- light to excite specific transitions from the m_{F}=0 state which become in resonant as the effective detuning goes to zero in Eq. 2.20. The combined force for a 1-D MOT, to first order in the Doppler and Zeeman effects, is given by,

$$F = 8\hbar k \frac{s_o(\delta/\gamma)}{(1 + s_o + (2\delta/\gamma)^2)^2} (kv - (g_{\mathrm{F}'} m_{\mathrm{F}'} - g_{\mathrm{F}} m_{\mathrm{F}}) \mu_B \frac{dB}{dz} z/\hbar). \tag{2.21}$$

2.3.3 Magnetic Trap

Now that we have a complete Magneto-Optical Trap which can capture atoms from a thermal background, we can load these cooled atoms into a magnetic trap. To accomplish this, we simply turn off the lasers and increase the current in the quadrupole coils. While the magnetic force

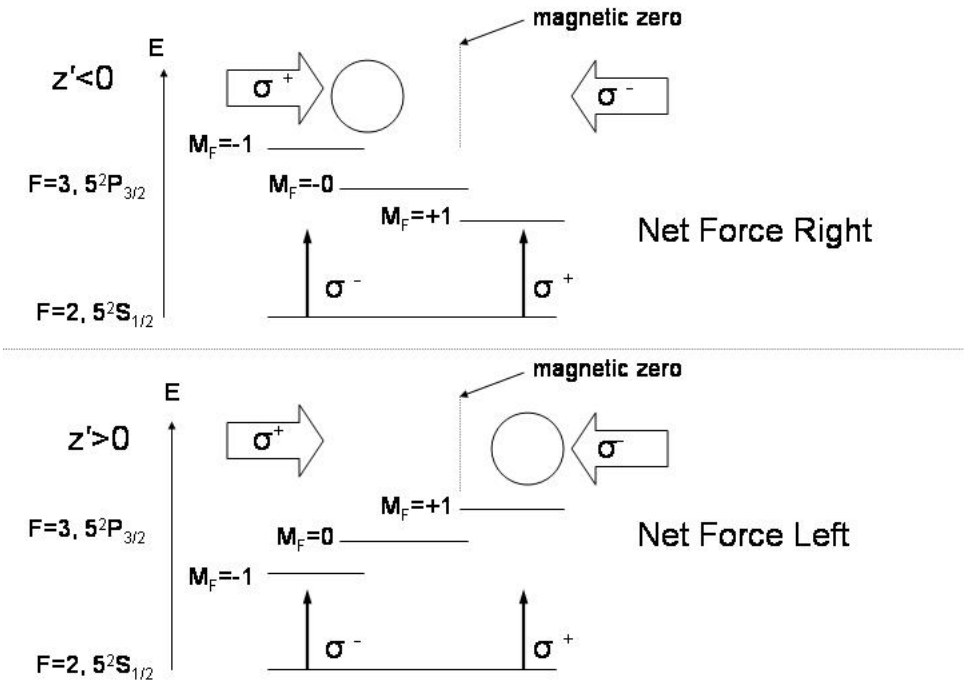

Figure 2.2: 1-D representation of the position dependant trapping force of a Magneto-Optical Trap. As a trapped rubidium atom moves to the left ($z < 0$) of the position of zero magnetic field, the σ^+ light becomes effectively much closer to resonance this causes a greater scattering rate from the left and hence a net force to the right. Similarly, if an atom is right ($z > 0$)of the zero, it exhibits a greater scattering rate from the σ^- polarized light and hence a net force to the left.

generated by our coils may not be sufficient to load as significant amount of atoms from the thermal background, we can easily transfer atoms from the MOT and hold them against gravity. Because the spin states play an important role to this trapping system, we will now discuss specific application to ^{87}Rb. The magnetic force on the atoms is

$$F_{\mathrm{mag}} \quad = \quad -\mu_{\mathrm{B}} g_{\mathrm{F}} m_{\mathrm{F}} \frac{dB}{dz}, \tag{2.22}$$

where the m_{F} values are the spin projection on the axis of the magnetic field. The states that may be held against gravity are states where the total force opposes gravity, or when the product of $g_{\mathrm{F}} m_{\mathrm{F}}$ is negative. We call these states magnetically trappable, and for the case of ^{87}Rb ground state, these are $|F = 2, m_{\mathrm{F}} = 2, 1 >$ and $|F = 1, m_{\mathrm{F}} = -1 >$. It is important to consider the effects of the Majorana spin-flip which impact trap loss in a quadrupole magnetic field due to the inherent magnetic field zero [13]. Under these spin-flip transitions, atoms that explore the magnetic field zero would see a rapidly changing magnetic field and could undergo transitions to untrappable states. For our purposes, we will neglect these transitions on the basis that they occur significantly faster than the trap lifetimes we study. In further support of this, for atoms in our MOT (estimated at 40-100μK), the volume over which Majorana spin flip effects are probably is given by,

$$\frac{v \frac{dB}{dz}}{\omega_L B} \ll 1 \tag{2.23}$$

where v is the mean speed of trapped atoms in the MOT, and ω_L is the Larmor frequency. Under our conditions, this volume is significantly smaller than the volume of the magnetic trap, and thus supports our theory that these transitions are negligible. We estimate the trap depth, comparing Eq. 2.19 with the effect of gravity, which for our gradients estimates on the order of 1mK.

We now present the equations for a magnetic field from a circular loop, and discuss specific coil configurations. By applying the Biot-Savard law we arrive at the magnetic field at a point z above a loop of radius R, given by,

$$B_z(z, D) = \frac{\mu_0 I}{2\pi} \frac{R^2}{(R^2 + z^2)^{3/2}}, \tag{2.24}$$

where μ_0 is the permeability of free space, and I is the current in the loop. Generalizing this equation for an arbitrary point as depicted in Fig. 2.3, for a loop of radius R, a distance D from the origin, the field can be expanded as a linear power series near the origin,

$$B_z(R, d, z, \rho) = \mu_0 I \frac{1}{2} \frac{R^2}{(D^2 + R^2)^{3/2}} + \mu_0 I \frac{3}{2} \frac{DR^2}{(D^2 + R^2)^{5/2}} z \tag{2.25}$$

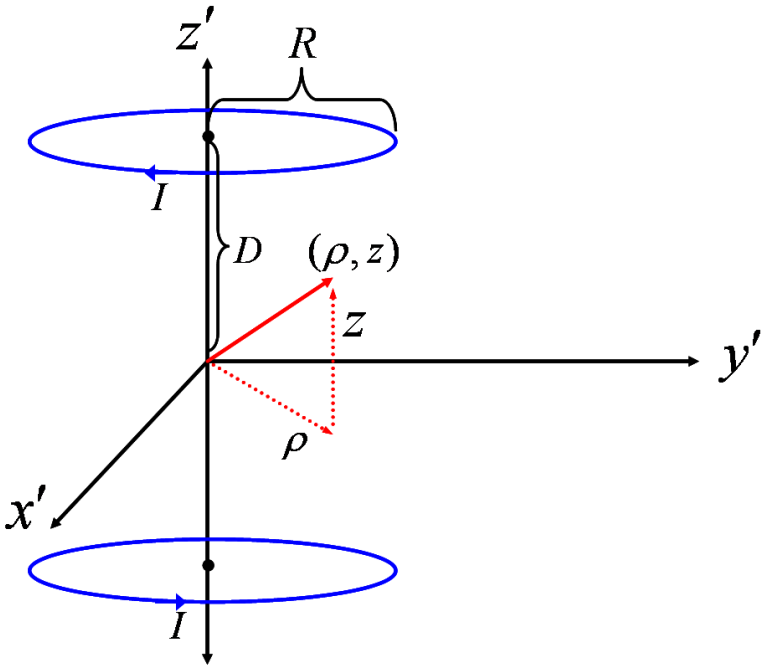

Figure 2.3: Two identical loops are shown in Anti-Helmholtz configuration with current I, radius R, with each positioned a distance D from the origin. The combined magnetic field from both loops at an arbitrary point (ρ,z) can be calculated using a Taylor expansion for points near the origin, and exactly in the case where $\rho = 0$.

$$B_p(R, d, z, \rho) = -\mu_0 I \frac{3}{4} \frac{DR^2}{(D^2 + R^2)^{5/2}} \rho \tag{2.26}$$

where z is the axial distance along the coil axes, and ρ is the radial distance. You can immediately see that this equation reduces to that of Eq. 2.24 for the case of z and $\rho = 0$, and that the radial gradient is half that of the axial gradient. Our exact configuration, coil dimensions and current are detailed in the Experimental Methods section to come.

Unlike the Helmholtz configuration, which is used to approximate a uniform field, the anti-Helmholtz configuration produces a magnetic field zero at the centre of the two coils, and a maximum axial gradient given by,

$$B_z(R, d, z, \rho) = 3\mu_0 I \frac{DR^2}{(D^2 + R^2)^{5/2}} z, \tag{2.27}$$

and radial gradient,

$$B_p(R, d, z, \rho) = -\mu_0 I \frac{3}{2} \frac{DR^2}{(D^2 + R^2)^{5/2}} \rho, \tag{2.28}$$

which is exactly half the axial gradient. The ideal anti-Helmholtz configuration maximizes gradient by setting $2D = R$, which is the same condition for the Helmholtz configuration to achieve a near uniform field.

2.4 Atom Rates

2.4.1 Atom Number Measurement

Now that we can trap atoms, we need a way of knowing how much we have trapped. In order to accomplish this, we can measure the amount of light coming from the atoms, using a variety of instruments including, a photomultiplier tube, a CCD camera, or a photodiode. In any of these cases we want to correlate the signal from scattered light with the number of atoms in the MOT. In order to estimate the light power emitted from the atoms, we ignore the interactions between scattered light and the atoms themselves, assuming the light travels radially outward in a uniform distribution. Given this assumption the fraction of light, f, hitting a lens is,

$$f = \frac{SA_{\text{lens}}}{SA_{\text{sphere}}} = \frac{r_{\text{lens}}^2}{d_{\text{lens}}^2}, \tag{2.29}$$

where r_{lens} is the radius of the lens and d_{lens} is the distance between the atoms and the lens. The

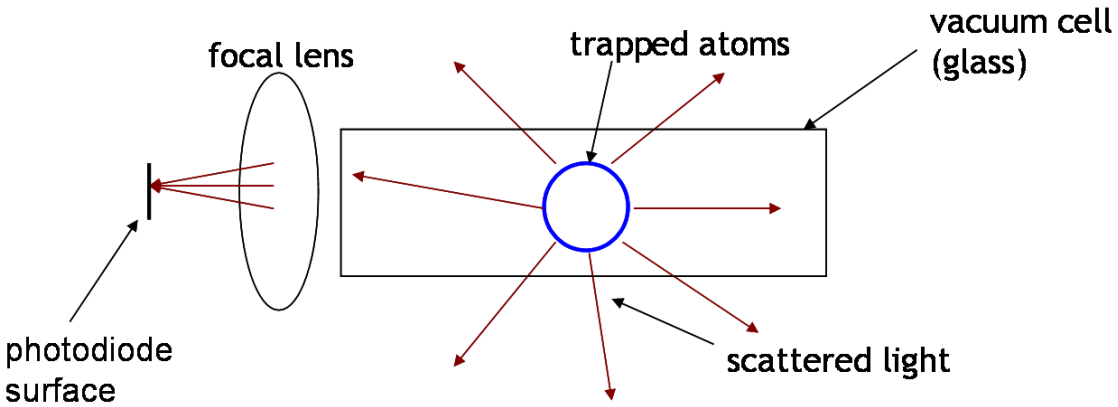

Figure 2.4: The process of scattered light, from the trapped atoms in the cell, reaching the photodiode is shown. The light emitted from spontaneous emission travels through the cell glass, and is then captured by a lens which focuses the light onto the surface of the photodiode. Through this method we can measure the number of atoms in the trap.

total light emitted from each atom is given by the scattering rate in Eq. 2.14, and if we assume a reflective loss on the cell glass of about 4% on both the inner and outer walls, the lens should receive a power of

$$P = h\nu \frac{r_{\text{lens}}^2}{d_{\text{lens}}^2} \quad R \quad N_{\text{atoms}}(.96)^2 \tag{2.30}$$

where N is the number of atoms in the MOT. One important thing to take away is that the predicted power emitted is linear with the number of atoms. An experimental calibration can then be done using the desired instrument in order to determine the output efficiency of $volts/Watt$. Using Eq. 2.30 and this calibration, we can then measure the approximate number of trapped atoms from their amount scattered light.

2.4.2 Rate Equations

Now that we can measure the number of atoms, we want to model how they atoms are loaded and lost from the trap. The atom number dynamics for an atomic species in the presence of a background vapour is modelled by the following rate equation [17]

$$\frac{dN}{dt} = \mathrm{R} - \Gamma N - \beta \int n_{\text{Rb}}^2 \, dV \tag{2.31}$$

$$R = \frac{2}{\pi} n_{\text{Rb}} A \frac{v_{\text{c}}^4}{v_{\text{th}}^3} \tag{2.32}$$

Where R is the loading rate which can be calculated following work done by Reif [33], Γ is the loss rate due to collisions between the trapped atoms of ^{87}Rb and the residual, room-temperature background gas, β the loss rate due to light-assisted collisions between trapped atoms of species ^{87}Rb, N is the trapped atom number of ^{87}Rb, and n_{Rb} is the density profile of ^{87}Rb. The loading rate predicted by classical kinetic theory, as given above, where n_{Rb} is the density of the gas to be loaded, A is the surface area of the trap and v_{c} is the velocity under which atoms will be captured by the trap. The mean speed given by the Maxwell-Boltzmann distribution v_{th} is

$$v_{\mathrm{th}} = \sqrt{\frac{8k_{\mathrm{B}}T}{\pi m_{\mathrm{Rb}}}}, \tag{2.33}$$

where m_{Rb} is the mass or rubidium, k_{B} is the Boltzmann constant, and T is the temperature of the background atoms (room temperature).

Making a constant density assumption for the β term, we can rewrite the integral term in Eq. 2.31 above as

$$\beta n_{\mathrm{Rb}}^2 \int dV = \beta \frac{N^2}{V^2} V = \beta' N^2 \tag{2.34}$$

where $\beta' = \beta/\mathrm{V}$ and V is the trap volume. From this assumption we can usually show for large Γ, the β integral term can be ignored. However, in high density situations, the term becomes important. If we include this term we can solve for the number of atoms as a function of time in the MOT assuming an initial condition corresponding to an empty trap. This gives

$$N(t) = N_\infty \frac{1 - e^{-\sqrt{\Gamma^2 + 4\,BR}\,t}}{1 + \frac{\beta' N_\infty^2}{R} e^{-\sqrt{\Gamma^2 + 4\beta' R}\,t}}, \tag{2.35}$$

where N_∞ is the number of atoms in the steady state,

$$N_\infty = \frac{\sqrt{\Gamma^2 + 4\beta' R} - \Gamma}{2\beta'}. \tag{2.36}$$

This fits well when the light assisted collisions are significant, but in the large Γ regime when the collisions become insignificant, the numerical fitting becomes challenging. In this case we revert to the simple case (assuming β=0), which gives,

$$N(t) = \frac{R}{\Gamma}(1 - e^{-t/\Gamma}). \tag{2.37}$$

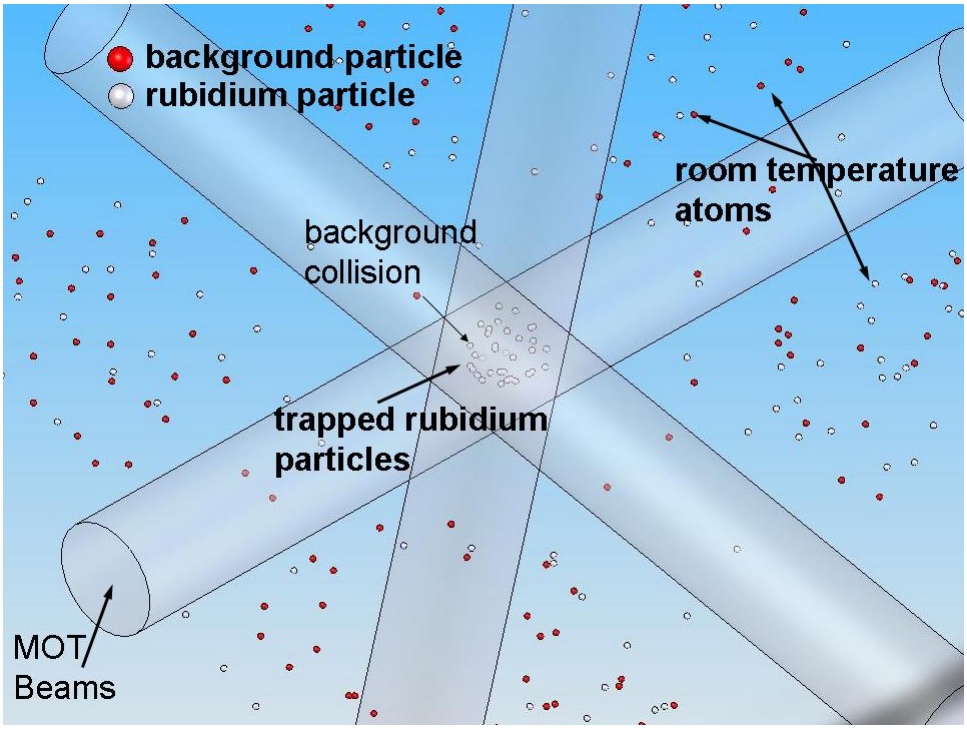

Figure 2.5: Representation of the vacuum chamber. Rubidium atoms with speed less than the capture velocity, v_c become trapped and held by the laser photons. Various gas species remain in the residual background of the chamber, the collisions between these atoms and the trapped atoms limits the lifetime of the magneto-optical and quadrupole magnetic trap.

2.4.3 Loss Rate and Elastic Cross Section

The loss rate due to collisions with the room temperature gas species is modelled as

$$\Gamma = \Gamma_{\mathrm{Rb}} + \Gamma_a + \Gamma_{\mathrm{residual}} \tag{2.38}$$

$$\Gamma_a = n_a \sigma_{\mathrm{Rb},a} \bar{v}_a, \tag{2.39}$$

where n_a is the gas density of the given species a, $\sigma_{\mathrm{Rb},a}$ is the collision cross section against rubidium atoms and $\bar{v}_a$ is the average speed of species a. We can assume the speed of the trapped atoms is negligible compared to the speed of the hot gas species which travel over 2 orders of magnitude faster. We usually separate the total loss rate due to collisions with hot gas molecules (Γ), into its components. Γ_{Rb} is the loss rate due to rubidium-rubidium collisions, Γ_a is from the collisions between trapped rubidium and the controlled background gas, and $\Gamma_{\mathrm{residual}}$ is the collisions with unwanted residual gas in the ultra-high vacuum. It is important to note as we change the controlled background gas density n_a, the slope in the total Γ is still given by $\sigma_{\mathrm{Rb},a}$ $\bar{v}_a$. FIG. 2.5 depicts the trapped atoms and the background atoms which will be involved in the collisions that make up Γ, the loss rate. Regarding the cross section, we need to consider recapture and the possibility that this is not an accurate measurement of the total cross section. The scattering theory related to this is presented in the subsection to follow.

For the cross section in the MOT, it is important to take note that we may be measuring the cross section of a combined mixture of different states. While in the MOT, we expected a steady state excited state fraction given by the corresponding density element in Eq. 2.12. Since it is possible that the cross section may differ significantly for the excited state, we will need to establish if our measurement is an accurate representation of the ground state cross section.

In the magnetic trap, the atoms are then held against gravity and confined in the trap until impacted by an atom from outside the trap. Instead of a loading rate equation, we have a decay rate equation which is simpler having only elastic collisions given by,

$$\frac{dN}{dt} = -\Gamma_{\mathrm{mt}} N. \tag{2.40}$$

where Γ_{mt} is just the loss rate due to elastic collisions with background gas in the magnetic trap. In this trap we only capture a portion of the original trapped atoms because not all atoms in the

MOT are in trappable states $|F = 2, m_{\rm F} = 2, 1 >$ or $|F = 1, m_{\rm F} = -1 >$. The solution to this equation becomes

$$N(t) \quad = \quad f e^{-t/\Gamma_{\rm mt}}, \tag{2.41}$$

where f is the initial fraction of atoms captured from the MOT. Similar to the MOT, $\Gamma_{\rm mt}$ is given by Eq. 2.39. This would seem to indicate the two loss rates should be the same, however, experimental evidence has shown that this is not the case. One possibility, is that the higher probability of recapture in the MOT causes a lower measured loss rate, which will be discussed in detail in the next section.

2.5 Scattering Theory

2.5.1 Classical Scattering

As a (hot) room-temperature particle interacts with a trapped particle in a MOT or magnetic trap, energy will be imparted to the trapped particle through elastic collisions. Classically, you expect two particles to collide as in Fig. 2.6 and impart energy given by the conservation of energy and momentum.

Starting from this picture, we can predict the velocity imparted by elastic collisions. The conservation equations are,

$$m_{\rm t}\vec{v}_t + m_{\rm Bg}\vec{v}_{\rm Bg} = m_{\rm t}\vec{v}_t\,' + m_{\rm Bg}\vec{v}_{\rm Bg}\,' \tag{2.42}$$

and

$$m_{\rm t}|\vec{v}_t|^2 + m_{\rm Bg}|\vec{v}_{\rm Bg}|^2 = m_{\rm t}|\vec{v}_t\,'|^2 + m_{\rm Bg}|\vec{v}_{\rm Bg}\,'|^2, \tag{2.43}$$

where $\vec{v}_t$ is the speed of the trapped particle, $\vec{v}_{\rm Bg}$ is the speed of the background particle, $m_{\rm Bg}$ is the mass of the background particle, $m_{\rm t}$ is the mass of the trapped particle, and the $'$ denotes the velocity after the collision. Introducing the relative velocity, $\vec{v}_r$ and velocity of the centre of mass, $\vec{v}_{cm}$ in terms of the reduced mass, μ as

$$\mu = \frac{m_{\rm t} m_{\rm Bg}}{m_{\rm t} + m_{\rm Bg}}, \tag{2.44}$$

$$\vec{v}_r = \vec{v}_{\rm Bg} - \vec{v}_t, \tag{2.45}$$

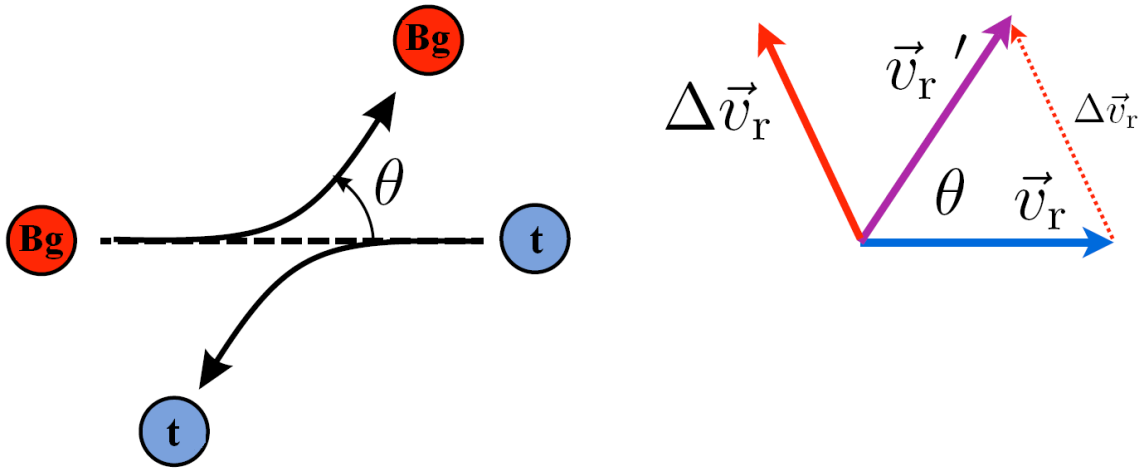

Figure 2.6: The collision of two particles is depicted classically, where θ is the scattering angle between the initial and final relative velocities. In our experiment we typically study collisions between a background (Bg) particle and trapped particle (t). The change in relative energy can lead to an estimate for the energy imparted in a collision.

and

$$\vec{v}_{cm} = \frac{\mu}{m_{\mathrm{Bg}}}\vec{v}_t + \frac{\mu}{m_{\mathrm{t}}}\vec{v}_{\mathrm{Bg}}, \tag{2.46}$$

we can rewrite the conservation equations as,

$$\vec{v}_{cm} = \vec{v}_{cm}\,' \tag{2.47}$$

and

$$\frac{|\vec{v}_r|^2}{m_{\mathrm{Bg}}} + \frac{|\vec{v}_r|^2}{m_{\mathrm{t}}} = \frac{|\vec{v}_r\,'|^2}{m_{\mathrm{Bg}}} + \frac{|\vec{v}_r\,'|^2}{m_{\mathrm{t}}}. \tag{2.48}$$

The first equation clearly shows that the speed of the centre of mass is conserved, and the second equation gives $|\vec{v}_r| = |\vec{v}_r\,'|$. To calculate the change in the relativity velocity, we use its definition,

$$|\Delta\vec{v}_r|^2 = |\vec{v}_r - \vec{v}_r\,'|^2 = |\vec{v}_r|^2 + |\vec{v}_r\,'|^2 + 2|\vec{v}_r||\vec{v}_r\,'|\cos\theta = 2|\vec{v}_r|^2(1-\cos\theta), \tag{2.49}$$

where θ is the scattering angle between the initial and final relative velocities.

Using this and the definition of $\Delta\vec{v}_r$, we can solve for the change of the trapped particle $\Delta\vec{v}_t$ using conservation of momentum,

$$m_{\mathrm{t}}\Delta\vec{v}_t = -m_{\mathrm{Bg}}\Delta\vec{v}_{\mathrm{Bg}}, \tag{2.50}$$

and

$$\Delta\vec{v}_t = \Delta\vec{v}_{\mathrm{Bg}} - \Delta\vec{v}_r = -\frac{\mu}{m_{\mathrm{t}}}\Delta\vec{v}_r. \tag{2.51}$$

We find the change in energy of the trapped atom for a given scattering angle,

$$\Delta E_t(\theta) = \frac{1}{2}m_{\mathrm{t}}(|\vec{v}_t + \Delta\vec{v}_t|^2 - |\vec{v}_t|^2), \tag{2.52}$$

which in the limit of vanishing initial kinetic energy ($|\vec{v}_t| \ll |\Delta\vec{v}_t|$) becomes,

$$\Delta E_t(\theta) \approx \frac{\mu^2}{m_{\mathrm{t}}}|\vec{v}_r|^2(1-\cos\theta), \tag{2.53}$$

where we have applied Eq. 2.49 and Eq. 2.51.

In order for an atom to escape the trap, it must be imparted energy larger than the trap depth U_0. This will be used in our calculation of the measured cross section as a function of trap depth in the sections that follow.

2.5.2 Quantum Scattering Theory

In order to predict theoretical values for cross sections, as well as to predict differences between the trap types, we present some formal definitions from quantum scattering theory. By writing the Schrodinger equation from Eq. 2.1 for two particles in the centre of mass frame for which we look for stationary solutions similar to Eq. 2.2. In order to calculate the total elastic cross section it is convenient to start with the differential cross section, defined as the number of particles scattered into an element of solid angle $d\sigma/d\Omega$ per unit time. This is usually defined in terms of the scattering amplitude $f(k,\theta)$ as,

$$\frac{d\sigma}{d\Omega} = |f(k,\theta)|^2 \tag{2.54}$$

where $k = \mu|\vec{v}_r|/\hbar = 2\pi/\lambda_{\mathrm{deBroglie}}$ is the collision wave vector, and we have assumed an istropic potential so that the scattering amplitude is independent of ϕ. The angle θ is the same angle discussed in the classical description. The scattering amplitude, $f(k,\theta)$ is defined by the asymptotic form of the wave function,

$$\psi(r) \approx A\left(e^{ikz} + f(k,\theta)\frac{e^{ikr}}{r}\right), \tag{2.55}$$

which is the sum of a plane wave (incident) and spherical (scattered) wave. Physically $f(k,\theta)$ is the amplitude of the asymptotic outgoing wave, which is depicted in Fig. 2.7. As is shown

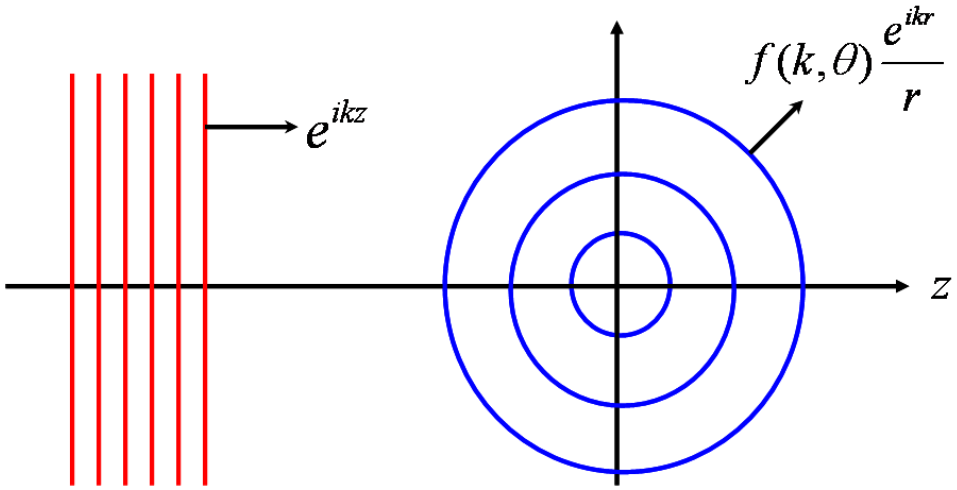

Figure 2.7: An incoming plane wave scattering off a potential to an outgoing spherical wave is depicted. This is the asymptotic form of the wave function expected from scattering theory, where the amplitude of the outgoing wave is $f(k,\theta)$ which is referred to as the scattering amplitude.

in many quantum mechanics textbooks [23], given a central potential, we can expand the wave function in the basis of Legendre polynomials as,

$$\Psi(r,\theta) = \sum_{l=0}^{\infty} R_l(k,r) P_l(\cos\theta) \tag{2.56}$$

where R_l is the radial part of the wave function which satisfies the radial wave equation. Similarly we expand $f(k,\theta)$ into a Legendre series as well. This is usually referred to as the partial wave expansion. In the limit as r gets large the solutions are the spherical Bessel (j_l) and Neumann (n_l) functions, so the general solution to the radial part is

$$R_l(k,r) = B_l j_l(kr) + C_l n_l(kr). \tag{2.57}$$

We then define the phase shift of each partial wave $\delta_l(k)$ as,

$$\delta_l(k) = arctan(-C_l/B_l) \tag{2.58}$$

as shown in Notes on Scattering Theory [32]. This results in an expression for the scattering amplitude,

$$f(k,\theta) = \frac{1}{k}\sum_{l=0}^{\infty}(2l+1)e^{i\delta_l}\sin\delta_l P_l(\cos\theta) \tag{2.59}$$

where we have expanded into a Legendre series. The only thing left to accomplish is the numerical determination of phase shifts for each of the partial waves, which has been studied previously [32]. It is convenient to introduce the complex T-matrix,

$$T_l(k) \equiv e^{i\delta_l} \sin \delta_l, \tag{2.60}$$

complex S-matrix (*scattering matrix*),

$$S_l(k) \equiv e^{2i\delta_l} = 1 + 2iT_l \tag{2.61}$$

and the real K-matrix,

$$K_l(k) \equiv \tan \delta_l(k) = -C_l/B_l, \tag{2.62}$$

from Eq. 2.58. Using basic complex substitutions, the relation between K and S is found,

$$S_l(k) = \frac{1 + iK_l}{1 - iK_l}. \tag{2.63}$$

We begin with the radial equation,

$$\left[\frac{d^2}{dr^2} + W(r)\right] \psi_l(r) = 0 \tag{2.64}$$

where

$$W(r) = k^2 - \frac{2\mu}{\hbar^2} V_{eff}(r, l), \tag{2.65}$$

$$V_{eff}(r, l) = V(r) + \frac{\hbar^2 l(l+1)}{2\mu r^2} \tag{2.66}$$

$$\psi_l(r) = kr R_l(r). \tag{2.67}$$

This allows us to calculate the phase shift for each partial wave as given by the asymptotic formula in Eq. 2.58 and hence the scattering amplitude and cross section. Details on the numerical calculation for this will be detailed in a later section describing the numerical methods. With this in hand, we can then integrate to get the total elastic cross section, given by

$$\sigma(k) = 2\pi \int_0^\pi |f(k, \theta)|^2 d\theta \tag{2.68}$$

where θ is again the scattering angle, and it is assumed all elastic collisions result in loss from the trap ($U_0 = 0$).

2.5.3 Cross section dependence on trap depth

For different trap depths, there is the possibility that atoms can undergo collisions and remain trapped. If the energy transferred to the particle is not sufficient for the particle to escape the trap, it may remain trapped and the collision will not be detected experimentally by the loss of that particle. In order to calculate the cross section for various trap depths, we need to determine the minimum scattering angle that causes trap loss, usually referred to as the scattering angle resolution. The speed transferred to the trapped (Rb) particle is given in Eq. 2.53 which we invert to calculate the scattering angle resolution for a given trap depth (U_0) as,

$$\theta_r = \cos^{-1}\left(1 - \frac{U_o m_t}{\mu^2 v_r^2}\right) \tag{2.69}$$

where θ_r is between 0 (perfect resolution) and π (zero resolution). We can then calculate a loss cross section, assuming that collisions above the scattering angle resolution are resolved (observed) as particle loss from the trap, this is hence

$$\sigma_{\text{loss}}(k) = 2\pi \int_{\theta_r}^{\pi} |f(k,\theta)|^2 d\theta. \tag{2.70}$$

With this estimate in hand, we can compare the measured cross sections from the different trap types and compare the theoretical values for the corresponding trap depths to see if they follow the theoretical predictions.

2.6 Trap Depth Estimation

As we will show, the cross section has a significant difference between the MOT trap depth and magnetic trap depth, and as a result, to compare our experimental results, we want to estimate the experimental trap depths.

2.6.1 Magnetic Trap Depth

This is easy to do for the magnetic trap, in which we can vary the trap depth by driving various currents through the coils. By using the magnetic field equations presented in Eq. 2.27 and Eq. 2.28 we can predict the energy required to escape the trap along different trajectories. Assuming the atom explores a significant region within the trap, a good assumption is the minimum trap

depth. Denoting the axial gradient as $\frac{dB}{dz}$, where to first order,

$$\frac{dB}{dz} = \mu_0 I \frac{3}{2} \frac{DR^2}{(D^2 + R^2)^{5/2}}, \tag{2.71}$$

we calculate the minimum axial trap depth (U_0^{axial}) against gravity as,

$$U_0^{\text{axial}} = \left(\frac{dB}{dz} - m_{\text{t}} g \right) z_{\text{wall}}, \tag{2.72}$$

where z_{wall} is evaluated as the distance to the wall of the cell (5 mm). We compare this with the radial trap depth, where the gradient is half the axial gradient,

$$U_0^{\text{radial}} = \frac{1}{2} \frac{dB}{dz} z_{\text{wall}}. \tag{2.73}$$

We expect the effective trap depth to be somewhere between these two values and this will be what we use to compare experimental cross sections with theoretical as a function of trap depth. It should be noted here that we will also present an experimental verification of the estimated theoretical gradient in the experimental results chapter.

Chapter 3

Experimental Methods

This chapter details the experimental components and methods used to perform the experimental measurements. A 3-d model of the experiment is shown in Fig. 3.1. The other components not shown are typically not in use while performing collision cross-section measurements, which are the key focus of this thesis.

3.1 Vacuum System

This section will detail the vacuum system and various components related to vacuum measurements and control. This is key to the thesis as we are primarily interested in how loss rates vary with the residual background gas in the vacuum.

3.1.1 Pumps

Our vacuum system relies on three types of pumps, an ion-pump, getters, and a turbomolecular pump. Each of these has a different use and supports the overall goal of maintaining a consistent vacuum. A simple description of each type of pump and its advantages will be presented in addition to the specific models we use in our system.

The ion-pump has no moving parts and performs pumping by ionizing the background gas and using a large electric field and magnetic field to accelerate these ions to a solid electrode. We use the Thermionics IP-011 ion pump which has a rated pump speed of 11L/sec and weighs about 14 lb. As a side-project to our experiment, the lab plans to further miniaturize our experimental setup, and is still investigating ways to remove the ion pump while still maintaining UHV conditions in a sealed vacuum cell. When performing collision cross-section measurements, the ion pump is turned off since these devices also ionize the background gas and, its use leads to a pressure differential between the trapping region and the pressure measurement region of the vacuum system.

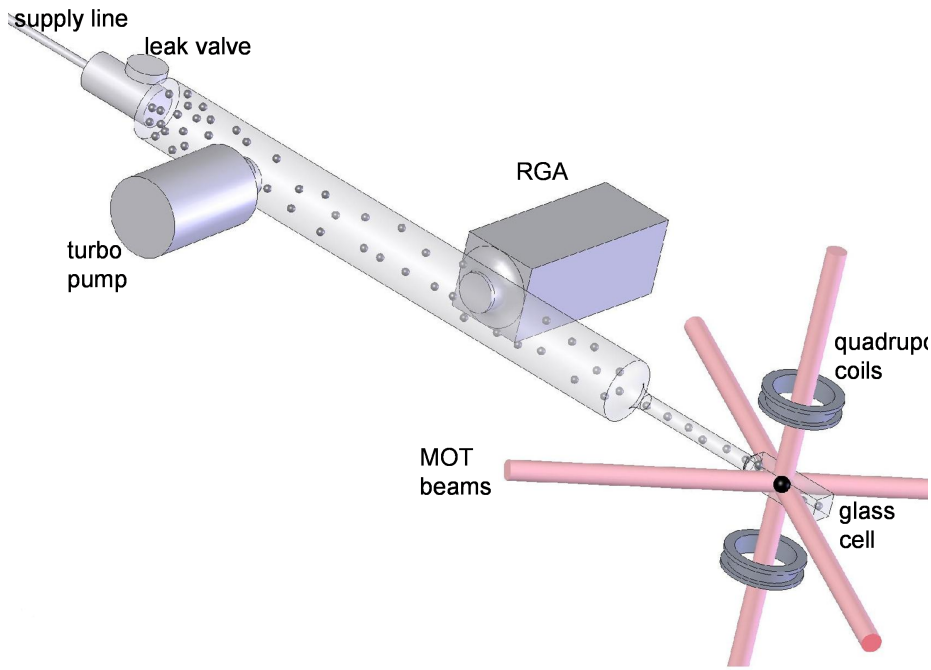

Figure 3.1: An overview of the experiment is presented with the devices that are used while performing collision cross section measurements. The leak valve is used to increase the background pressure of a given species a from a supply tank, the turbo pump helps maintain the vacuum stability, and the residual gas analyzer performs the required pressure measurements. The loss rate in the magneto-optical and magnetic traps are measured as a function of background pressure.

In contrast to the ion-pump, the turbomolecular pump (turbo-pump) uses several layers of spinning rotor blades to give directional momentum to atoms in the chamber drawing them to an exhaust region. The model used is a Varian turbo pump (Turbo-V 81) with pumping speeds that vary depending on the background gas but are usually around 50L/sec which is significantly higher than the speed produced by the ion-pump. This model also suffers from poor portability, weighing about 5lb and requires a mechanical pump to pump away the compressed gases from the exhaust port of the turbo-pump. Compression ratios for the turbo-pump also vary depending on the gas, and the pump is significantly better for pumping nitrogen as compared to hydrogen. This is the only pump we will leave on while performing collision cross section measurements as we leak in a desired gas (argon or helium) and study the MOT/magnetic trap loss rates.

The third type of pump used is a chemical getter pump. This is a compact pump (1.2 cm diameter and 10cm length) which has no moving parts and, once activated, requires no external power. The getter pump relies on a chemical reaction between the pumps active material and the background gas to maintain the low pressure in the cell. These pumps continually pump nitrogen, hydrogen, oxygen, and methane, but cannot pump noble gases.

3.1.2 Source

Rubidium vapour is introduced to the test chamber by heating a commercially available alkali vapour source (Alvatec As-2-Rb-25-V). This model has a diameter of 2mm and contains 25mg of rubidium. Since the ion pump and turbo-pumps remove rubidium vapour from the vacuum system over time, it is replenished by electrically heating the getter. The getter begins to emit rubidium vapour at a current of 4.0A and the flux increases with current (power). Typically, rubidium vapour is added after each 8 hour data collection run by setting the current to the getter to 5.0A for 2 3 minutes. The rubidium pressure is allowed to equilibrate for 12-14 hours before a new data set can be collected.

3.1.3 Leak Valve

The focus of this thesis relies on introducing a specific gas through a variable leak valve [Varian model 9515196]. This increases the equilibrium pressure of this gas in the trapping region and hence the loss rate from the MOT and magnetic traps is also increased. We record the loss rate as a function of the gas pressure to deduce the collisional cross-section between the specific gas

and ^{87}Rb for both trap types. We chose helium and argon to study initially because they have been previously measured and being inert, have few complications with our vacuum system.

3.1.4 Pressure Measurement

In order to extract the cross section from the loss rate using Eq. 2.39, we need to measure the density, or pressure of the background gas. In this pressure regime there are at least two commonly used devices; the residual gas analyzer (RGA) and the ion gauge. These both work on the same principle of ionizing the background gases and detecting the ions. The RGA has a mass spectrometer which allows it to indicate the various partial pressures. Since both devices rely on ionization, their calibration factor for each type of gas will vary. Upon investigation into both these devices, it has become clear that the manufacturer did not attempt to claim a quantitative accuracy on the measurement, and it is important to be skeptical of the pressure reported by either of these devices. We have also begun exploring a calibration of the RGA using a gas expansion technique; a high pressure (several Torr) of He or Ar is introduced into a small volume region attached to the test chamber. This pressure is measured using a capacitance manometer (Baratron) accurate to 1%. The gas is then expanded several times to a low pressure that is calculated based on the volume ratio between the original volume and the test system. The calculated pressure is compared with the pressure read using the RGA for the calibration. This work is currently under way.

3.2 Imaging Instruments

In our experiment we have explored the use of a photodiode, and CCD Camera. Although each has its advantages, for the majority of our measurements we rely primarily on the photodiode. The goal of these detectors is to monitor the MOT, both for alignment purposes, and the primary reason of tracking trapped atom numbers.

3.2.1 Photodiode

These instruments both detect the amount of incoming light and output a current/voltage to describe the amount of light. Although they perform similar operations, they vary in principle and also have different signal-noise ratios (SNR) for various light intensities, and experimentally

we find the photodiode slightly better. These are excellent for our measurement of MOT scattered light and hence useful for measuring atom numbers on short (ms to minute time scales). In order to measure the light coming from the cell, we use a focusing lens to capture the scattered light and focus it onto the photodiode. The efficiency of capture has been described in the theory chapter and is summarized in Eq. 2.30. We can calculate the atom number based on an experimental calibration of efficiency of power to voltage output, however this does not affect our key results since power is linear with the number of atoms and we only care about changes in atom number. The photodiode signal is recorded over time using an oscilloscope which is then sent to and recorded on a lab computer using LabVIEW. This provides the complete description for measuring atom loss rates for a given background pressure.

3.2.2 CCD Camera

The CCD Camera has some advantages over the photodiode, the main one being that information becomes two-dimensional. This allows us to have a better idea on the shape of the MOT and how the atoms are behaving in the trap. Although this is not used explicitly in calculating our results it is extremely useful in aiding alignment of the MOT and in studying the atoms behaviour under various conditions. It is also used for absorptive imaging of the cold atom cloud to allow us to determine the temperature of the atoms (40-100 μK). Overall, the CCD Camera is only useful qualitatively for our experiment and it is not beneficial to discuss various methods of pixel summing or fitting the trapped atoms to a Gaussian.

3.3 Laser System

The laser system used in this thesis has been well detailed previously, and for the purposes of this thesis is not a main focus[22].

3.3.1 Rubidium Transitions

Since we are primarily focused on trapping isotopes of Rubidium, we will discuss the specific details required to create a Magneto-Optical trap. For both ^{87}Rb and ^{85}Rb, the atom is not a simple two-level system as described in the Theory chapter of this thesis. To undergo the usual cooling, we setup a laser tuned to the transition of a ground state to an excited state, which

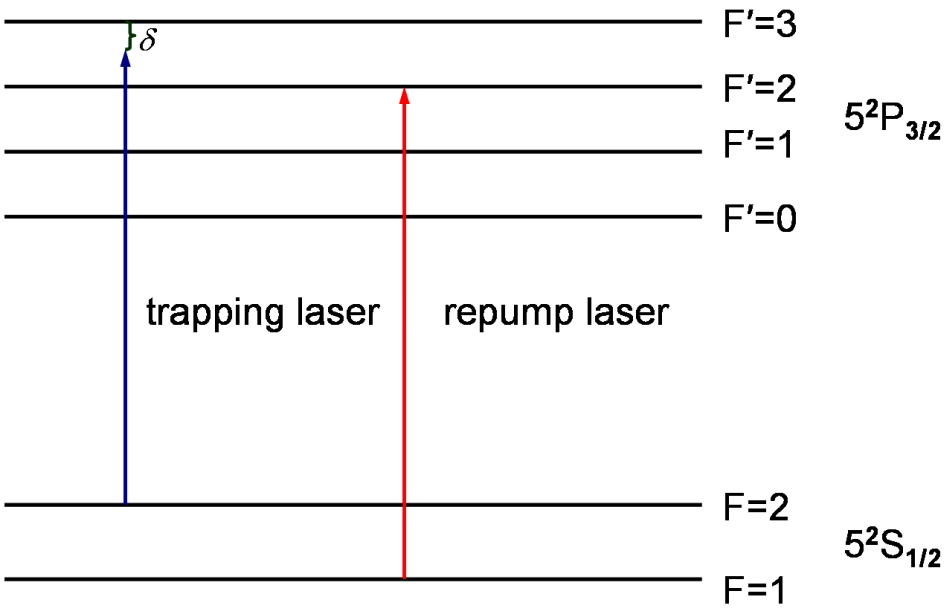

Figure 3.2: The energy levels of ^{87}Rb are shown above for the hyperfine levels of the ground and excited states. The trapping laser with detuning δ excites atoms from the $|F = 2>$ ground state to the $|F' = 3>$ excited state which results in cooling. After undergoing spontaneous emission from the excited state, particles may decay to both hyperfine levels of the ground state. Atoms that fall in the lower hyperfine state ($|F = 1>$) are transparent to the trapping laser, which requires need for a second laser known as the repump laser, tuned to a transition which allows spontaneous decay back to the $|F = 2>$ state.

allows for the atoms to absorb photons according to the scattering rate in Eq.2.14. As you can see in Fig 3.2 the atoms in higher ground state, $|F = 2>$ for ^{87}Rb and $|F = 3>$ for ^{85}Rb, are respectively transitioned to the $|F' = 3>$ and $|F' = 4>$ excited states. Due to the selection rules, the atoms can undergo spontaneous emission resulting in decay to either ground state [23]. This causes a problem as the atoms that fall to the lower ground state become transparent to the cooling laser. To avoid this situation we use a second laser, referred to as the repump laser, which is tuned to the transition of the lower ground state to an appropriate excited state which allows for spontaneous decay back to the higher ground state. This mechanism is fully described in the Fig. 3.2 for ^{87}Rb which clearly shows the two laser transitions and the relevant states.

3.3.2 Laser Detuning and Power

In Magneto-Optical traps, a wide range of detuning and power can be combined to create a successful trap. By using Acoustic Optical Modulators (AOMs) we shift the detuning of the cooling and repump lasers each by a detuning electronically controlled. Typically, in our experiment, we sit at a detuning around 2 linewidths, and around 20mW of laser power for a beam approximately 1 cm in diameter which is split among 3 retroflected beams. For experimental characterizations however, we will explore a range of detuning and power which will be shown in the Results section of this thesis. It is important to keep in mind the excited state fraction, given by Eq. 2.12, which may have a different loss rate and cross section and can lead to increased light-assisted collisions.

Even though the magnetic trap does not rely on laser light, the initial loading from the MOT uses light at a given detuning and power it is often convenient to rapidly load atoms in the MOT, and switch to a far detuned (4 linewidths) cooling beam which results in a colder distribution of atoms loaded into the magnetic trap. The light is again used when we want to measure how many atoms are left after a given time by flashing the lasers back on for a fluorescence measurement. During this process, we require the use of a mechanical shutter to fully block the light reaching the cell. Without the aid of the shutter, the scattered light from the AOMs is sufficient to send the atoms flying out of the trap. The shutter operation time has been tested to be less than 20ms, and it is important to take this delay into account when performing magnetic trapping routines.

3.4 Magnetic Coils

3.4.1 Coil Dimensions

A pair of coils were designed with many factors in mind, but have the main goal of achieving an effective magnetic trap without water cooling of the coils. These coils are in the anti-Helmholtz configuration described in the theory chapter of this thesis, and their dimensions are detailed in Fig. 3.3.

3.4.2 Exact Configuration

In order to predict trap depth, we need to be able to estimate the gradient of the magnetic coils. To do this we use a modified script written by Todd Meyrath [13] for calculating the magnetic

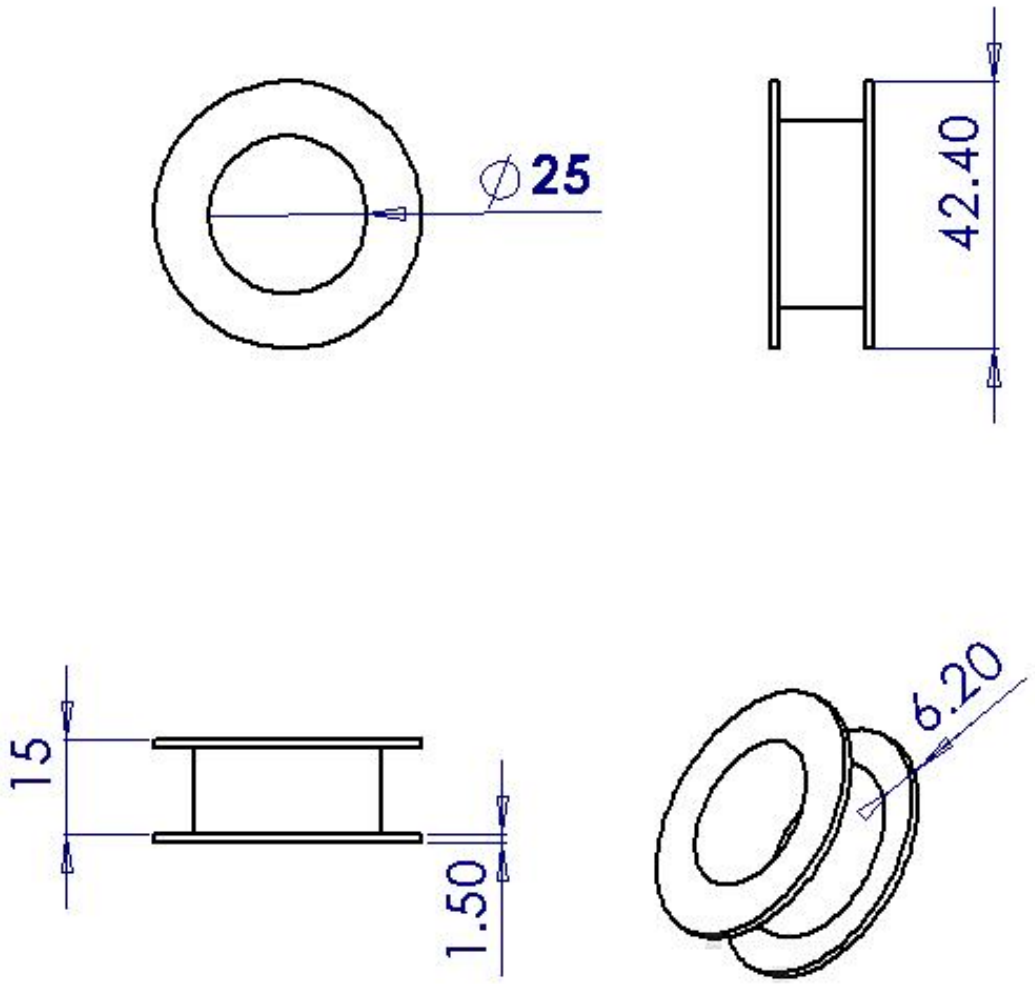

Figure 3.3: Model of one of the two identical magnetic coils used for both the magneto optical and magnetic traps, where the units are given in mm. These coils were constructed at the UBC machine shop this summer.

field at a point from a given set of coils. The magnetic field of the quadrupole pair is plotted as a function of z, the axial distance, as shown in Fig. 3.4. From the gradient estimated from this technique (3.46G/cm/A) we can estimate the magnetic trap depth in both the radial and axial directions as described by Eq. 2.72 and Eq. 2.73.

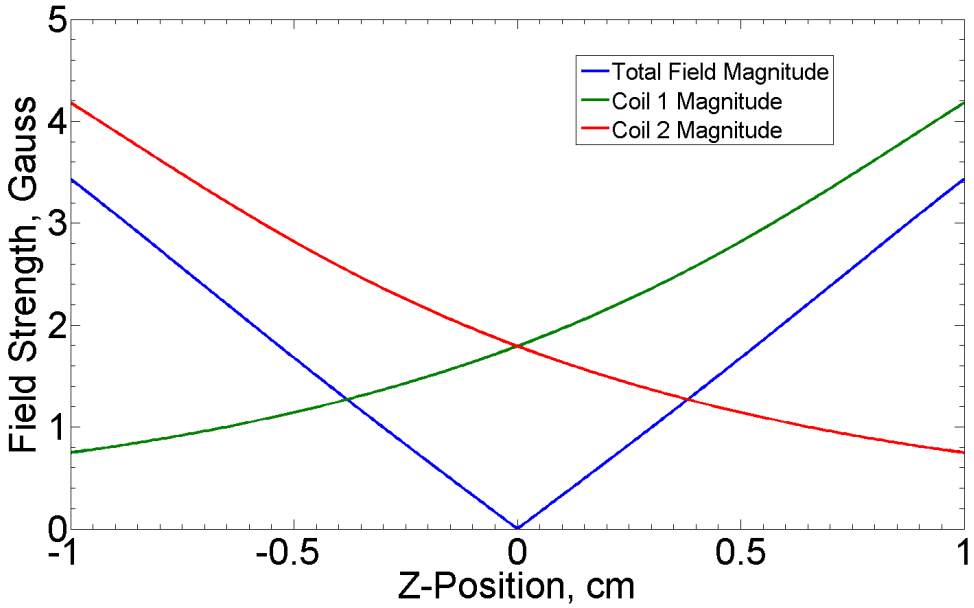

Figure 3.4: Theoretical estimate of the magnetic field generated by our quadrupole coils are shown, including the individual effects from each coil and combined effect from the pair, resulting in an estimated gradient of about 3.46G/cm/A. From this gradient we can predict the magnetic trap depth in both the radial and axial directions.

3.5 Electronic Control System

The combined control system will be briefly outlined in this section, as shown in Fig. 3.5. The intricate details of the implementation of the system was completed before I arrived at the Quantum Degenerate Gas laboratory, but has been detailed previously [22].

3.5.1 Hardware Control System

In order to perform the experimental measurements of interest we need to electronically control most of the components at speeds significantly faster than the human reaction time. Given our typical loss rates, loading rates and falling rates due to gravity, we require timing on the order of a millisecond. In order to accomplish this, a National Instruments Data Acquisition (NI-DAQ) card with a 20MHz clock rate is used, which sends single instructions over a UTBus Driver every clock cycle (20MHz). The UTBus is simply a parallel forwarding device which sends output to many devices, with a 32-bit address code specifying which device should handle the instruction.

Primary devices for our lab include the Direct Digital Synthesizers (DDS), Analog Output Device (AO), and Digital Output Device. These are used to control the various devices including the AOMs, mechanical shutters, oscilloscope trigger, and coil drivers.

3.5.2 Software Control System

For each measurement, we write a python script for controlling the necessary electronic devices. This is usually interfaced with a LabView routine which allows user input for various parameters. Generally, we run a LabVIEW script which will call necessary python routines and automatically record data from the oscilloscope (over ethernet), after which, the script performs optional fitting and file saving operations. This makes most of the experimental measurements automatable, except in cases where data is not digitally recorded (RGA, power meter, etc). Although LabVIEW is a useful tool, it has significant overhead, is not freely distributable on any computer, and working with a high-level programming language would be beneficial. The python script will generate bytecode which is interpreted by a C++ interface, and sent to the NI-DAQ card for execution over the UTBus.

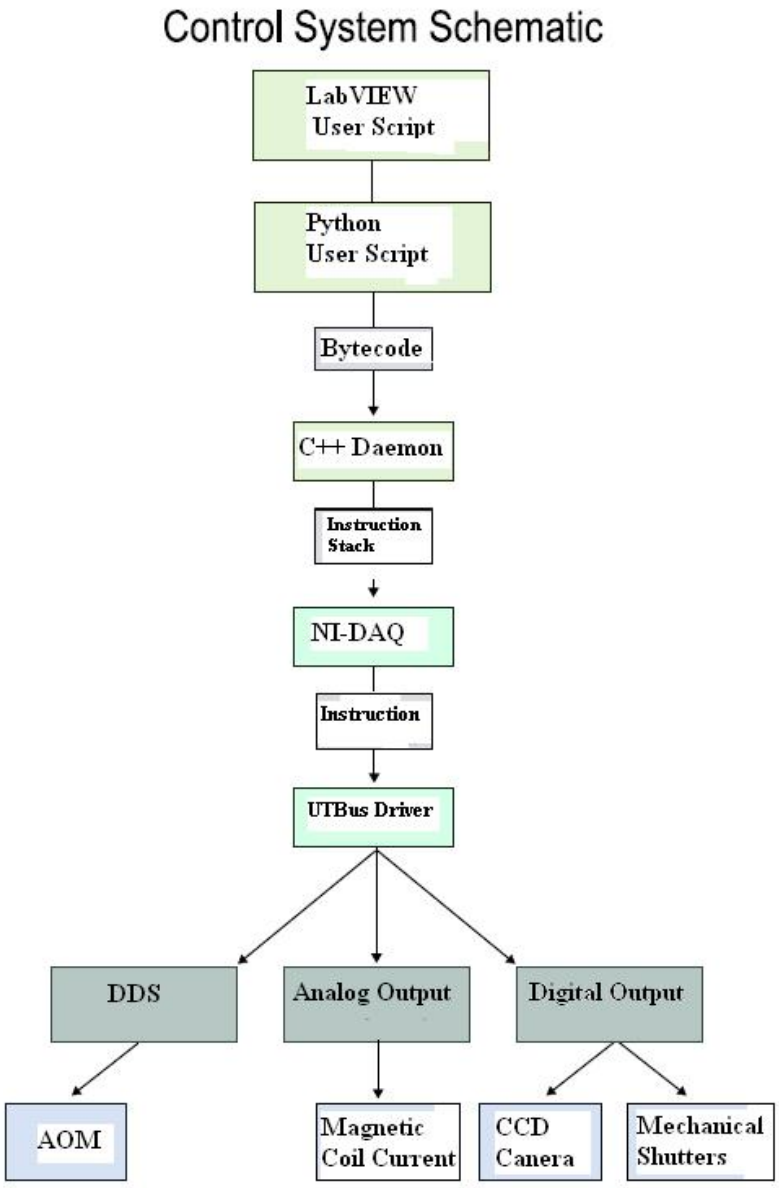

Figure 3.5: The control system for the experiment is depicted. The overall scheme is a hierarchy beginning with graphical and programming interfaces for user scripts, which are converted to bytecode and sent to the data acquisition (NI-DAQ) card which maintains an instruction stack. Each instruction is then carried out over the UTBus through various output devices which control the end devices in our experiment such as the magnetic coils and mechanical shutter.

Chapter 4

Numerical Methods

4.1 Total Elastic Cross Section

In order to begin calculations for the total elastic cross sections, we begin with the partial wave expansion described in the theory chapter of this thesis. By calculating the asymptotic form of the radial partial waves, we can extract information about the scattering amplitude $f(k, \theta)$.

4.1.1 Partial Waves

We implement a numerical technique to solve the radial equation asymptotic form (Eq. 2.64) for a given potential between two atoms. As outlined by B.R. Johnson [2 in Nicola], it is convenient to introduce the logarithmic derivative, y, of ψ,

$$y = \frac{\psi'}{\psi}. \tag{4.1}$$

This transforms the radial equation into,

$$y'(r) + y^2(r) + W(r) = 0, \tag{4.2}$$

which as shown by Johnson, can be integrated numerically using the formula

$$y_n = \frac{y_{n-1}}{1 + h y_{n-1}} - \frac{h}{3} w_n u_n, \tag{4.3}$$

where $y_n = y_0 + nh$, the subscript n indicates the integration step of step size h and should not be confused with the partial wave subscript l which will be used later. The potential comes in from u_n as,

$$u_n = \begin{cases} W(r_n), & n = 0, 2, 4, ..., N \\ \frac{W(r_n)}{1 + \frac{h^2}{6} W(r_n)}, & n = 1, 3, 5, ..., N - 1 \end{cases}, \tag{4.4}$$

with weights, w_n given by,

$$w_n = \begin{cases} 1, \ n = 0, N \\ 4, \ n = 1, 3, 5, ..., N-1 \\ 2, \ n = 2, 4, 6, ..., N-2 \end{cases}, \tag{4.5}$$

where N is the final integration step in the limit of large r. Integrating this from below one atomic unit, for a repulsive potential, we assume the wave function vanishes so we set the logarithmic derivative to a numerically large value. In the asymptotic limit, each partial wave can be expressed using Eq. 2.67 and the asymptotic limit described in 2.57 to give,

$$\psi_l(r) = B_l \left[\hat{j}_l(kr) - K_l \hat{n}_l(kr) \right], \tag{4.6}$$

where the Ricatti-Bessel functions are defined,

$$\hat{j}_l(kr) = kr j_l(kr), \tag{4.7}$$

$$\hat{n}_l(kr) = kr n_l(kr). \tag{4.8}$$

We can invert this relation by differentiating to solve for the K-matrix elements K_l (Eq. 4.9) and using the definition of the logarithmic derivative y in Eq. 4.1,

$$K_l = \frac{y_l \hat{j}_l - \hat{j}_l'}{y_l \hat{n}_l - \hat{n}_l'}. \tag{4.9}$$

From these elements we can find the T_l matrix elements using Eq. 2.61 and Eq. 2.60.

We can then replace the integral expression (Eq. 2.68) with a summation over T-matrix elements,

$$\sigma(k) = \frac{4\pi}{k} \sum_{l=0}^{\infty} (2l+1) |T_l(k)|^2. \tag{4.10}$$

Now that we have the cross section in terms of quantities we can calculate, we can write numerical code to perform the integration on y and summation of T-matrix elements over partial waves. This was coded in Fortran, however we will discuss the specific implementation parameters as well as numerical convergence and units.

4.1.2 Implementation Details

It is important to test the numerical calculation among different convergence situations. It is trivial to test that the solution is independent of the initial condition (large derivative in y), but it is important to test convergence of partial waves and integration range of r. For all the calculations included in this thesis, the logarithmic derivative initial condition is set to $y = 10^{30}$ and the grid range is usually 1 to 50 atomic units when convergence testing is successful. Convergence of partial waves is ensured simply by checking the magnitude of the $(2l+1)|T_l(k)|^2$ component to be a few orders of magnitude smaller than the desired precision.

Because of the nature of the calculation, checking convergence and independence of grid range needs to be implemented. For this thesis, code was originally automated to perform the calculation once, expand the grid, decrease the step size h, and compute the cross section again, and stopping when the change passes a desired threshold. For running time purposes, it was usually faster to estimate the necessary constraints before hand, and run the series of calculations.

To calculate the l-th order spherical Bessel and Neumann functions and their derivatives, we use the recipe provided by Numerical Recipes, for evaluation at a point. We then perform the necessary (small) adjustments to complete the calculation for the Ricatti-Bessel's functions.

This particular implementation also integrates the cross section of a given k (or associated velocity) over the Maxwell-Boltzmann speed distribution to get the expected total elastic cross section of a temperature distribution (here a simple midpoint rule integration was used). This results in an expression for the expected cross section of,

$$< \sigma >= 4\pi \int_0^\infty \left(\frac{m_{\mathrm{Bg}}}{2\pi k_B T}\right)^{3/2} v_{\mathrm{Bg}}^2 e^{-m_{\mathrm{Bg}} v_{\mathrm{Bg}}^2/(2k_B T)} \sigma(\mu|v_{\mathrm{Bg}}|/\hbar) dv_{\mathrm{Bg}}, \tag{4.11}$$

where T is the temperature of the background gas, k_B is the Boltzmann constant, and we check to ensure we have sufficient resolution and width sampling of the curve to ensure convergence in the cross section value. All calculations are done mostly in atomic units, but converted back into standard units for presentation and discussion.

4.1.3 Loss Rate Comparison

For comparison with experiment, however, we measure loss rates and extract a proportionality constant from the density. The equation presented in the theory section for the loss rate in Eq. 2.39 is a good approximation, but is better expressed as an integral over the Maxwell-Boltzmann

distribution as well. This becomes,

$$\Gamma \;=\; n_{\rm Bg} < \sigma v_{\rm Bg} >= 4\pi n_{\rm Bg} \int_0^\infty \left(\frac{m_{\rm Bg}}{2\pi k_B T}\right)^{3/2} v_{\rm Bg}^3 e^{-m_{\rm Bg} v_{\rm Bg}^2/(2k_B T)} \sigma(\mu |v_{\rm Bg}|/\hbar) dv_{\rm Bg}, \quad (4.12)$$

where $n_{\rm Bg}$ is the density of the background gas. Previously, we have compared $< \sigma >< v_{\rm Bg} >$ to the proportionality constant of the loss rate, and we can now compare the correct expression for the proportionality constant, $< \sigma v_{\rm Bg} >$ with the experimental values which will likely improve the accuracy of the loss rate prediction.

4.2 Partial Cross Section vs Trap Depth

As interest was originally primarily on the total cross section estimates, the code was already established to calculate T-matrix elements. In order to calculate the integral from a minimum scattering angle resolution as in Eq. 2.70, it is convenient to calculate the scattering amplitude from the T-matrix elements by Eq. 2.59 by noticing that it be written as,

$$f(k,\theta) = \frac{1}{k} \sum_{l=0}^{\infty} (2l+1) T_l(k) P_l(\cos\theta). \quad (4.13)$$

Hence by taking the elements we have already calculated in our calculation of total cross section, we can also calculate the scattering amplitude explicitly, and perform the cross section integral from a minimum scattering angle resolution θ_r for a given trap depth. Numerically, this is done by employing the Gauss-Legendre method of integration, which is useful for integrating polynomials (Legendre polynomials in our case). We use a recipe from Numerical Recipes in FORTRAN [31] to calculate the corresponding weights and abscissas (points at which to evaluate). For the simple integral from θ_r, we have verified numerically that a 200 point summation with this method maintains sufficient convergence $< .1\mathring{A}$, and the convergence for this part is independent of all parameters. The end result is that we evaluate the partial cross section at a given trap depth by,

$$\sigma(U_0, k) = \sum_{i=1}^{N} w_i 2\pi |f(k,\theta_i)|^2 \sin\theta_i, \quad (4.14)$$

where N is the desired resolution (usually 200), and θ_i and w_i are given by the abscissas and weights respectively returned from the Gauss-Legendre method. At this point we usually also integrate over the Maxwell-Boltzmann distribution as for the total cross section case, to obtain

the expected partial cross section ($< \sigma_{\text{loss}}(U_0) >$) for a given temperature distribution and trap depth U_0. We can also calculate the expected loss rate as a function of trap depth and background density by using Eq. 4.12 with the appropriate trap dependence as in Eq. 4.14.

4.3 Comments

We can now calculate the cross section for a given temperature (energy) distribution or at a single collision speed, at an arbitrary trap depth. The only input the program requires in addition to these is the mass of the interacting particles as well as the potential describing their interaction (we will use a Leonard-Jones potential) which we define in the form,

$$V = \frac{C_{12}}{r^{12}} - \frac{C_6}{r^6} \tag{4.15}$$

which combines repulsive and attractive terms. It has been shown previously[30] that the cross section can be expressed as

$$\sigma(k) = A \left(\frac{C_6}{v} \right)^{2/(s-1)}, \tag{4.16}$$

where s is the power of the attractive term (s=6 in this case), and the result is independant of the short range, repulsive, term. We will verify this relationship in the numerical results chapter of this thesis, and discuss impacts of the C_{12} coefficient.

Chapter 5

Experimental Results

This chapter will detail the process used to extract the cross section, and show experimental samples of the steps used along the process.

5.1 Magneto-Optical Trap

In the MOT, the first step in the process is to study the loading of atoms as a function of time for a given background pressure (density). Typically, we begin with a fully loaded MOT, turn off the magnetic coils and turn the coils back up (50ms later). Plotting the fluorescence signal against time, we expect the loading rate to follow Eq. 2.37. As shown in Fig. 5.1, which contains a sample MOT loading curve taken during a ^{87}Rb-Ar collision cross section measurement, the model fits very nicely to the experimental data. The loss rate at a given background density is determined by the exponential constant, Γ averaged over several curves. At this point we then leak in more of the desired gas (argon or helium) and measure the loss rate at the new density. Repeating this process for several densities, we can plot the loss rate as a function of gas density, as shown in Fig.5.2. This allows us to extract both $< \sigma v >$ (loss rate slope), and an estimated cross section as shown later in Table 5.1. For comparisons with the theoretical results it will be more accurate to compare the loss rate slope with the theoretical values predicted for $< \sigma v >$.

5.2 Magnetic Trap

In the magnetic trap measurement, we load a fraction (usually 30-50 %) of the MOT trapped atoms into the magnetic trap, and measure the decay over time as they undergo elastic collisions with the background. The process is otherwise the same as the MOT and we begin by plotting the trapped fraction against time as shown in Fig. 5.3. For the magnetic trap, the rate model equation is simpler, having no light-assisted collisions, as described in Eq. 2.41. The fraction of trapped atoms that remain at a given time is measured by loading the magnetic trap, waiting

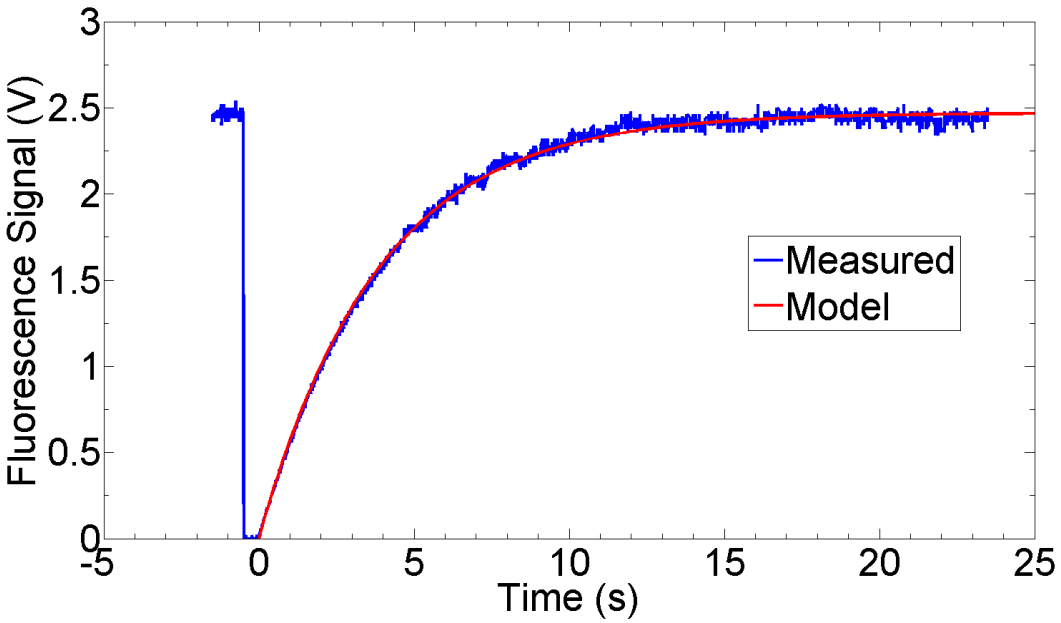

Figure 5.1: A sample loading curve of the magneto-optical trap is shown for ^{87}Rb. The atom number is measured using the fluorescence light scattered by trapped atoms, and plotted as a function of time from when the coils stabilized at normal operating current. Below initial time (t=0), the full level of the trap is shown. The measured loss rate is extracted from an exponential decay fit to the signal.

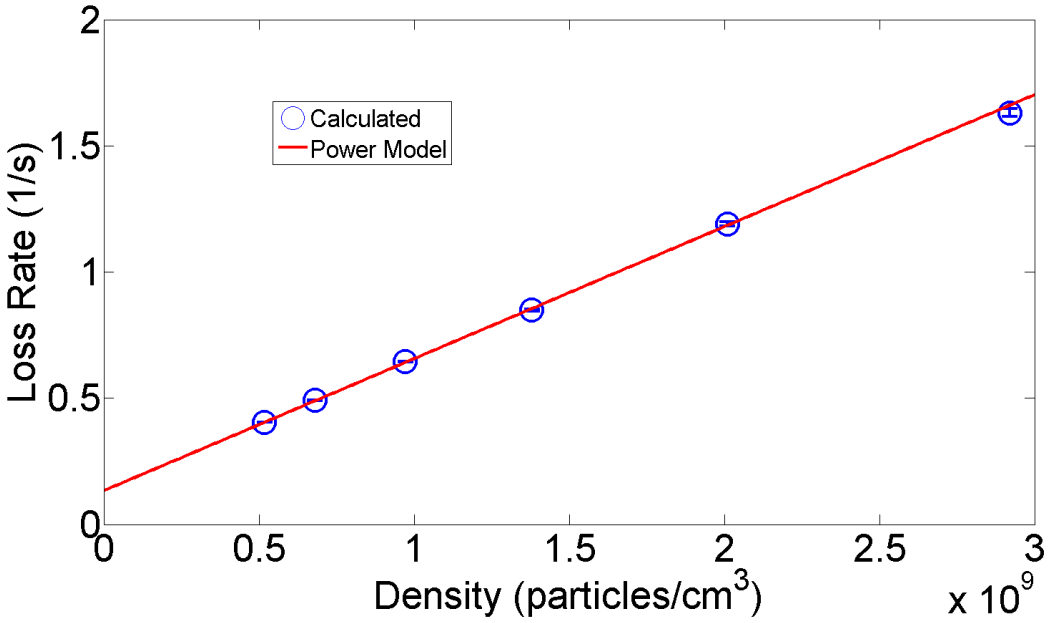

Figure 5.2: The loss rate in the magneto-optical trap (MOT) is plotted over varying background density, where increased background density results in more elastic collisions, and hence increased loss rate. The sample plot shown is for a MOT loaded with ^{87}Rb with increasing background argon density. The cross section can then be extracted from a linear fit to the loss rate.

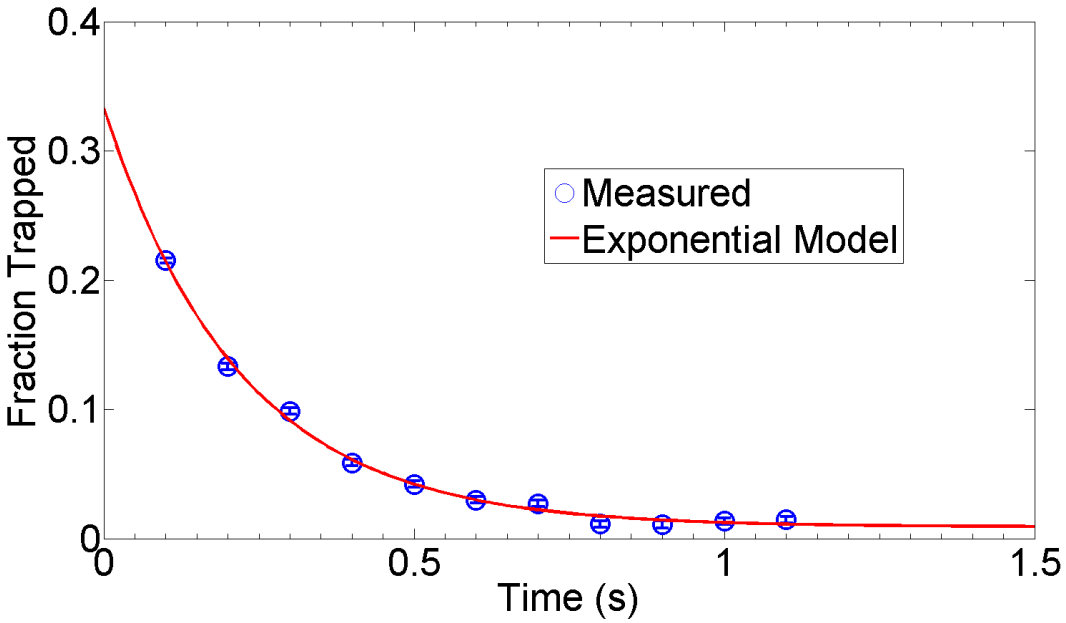

Figure 5.3: A sample decay curve of the magnetic trap is shown for ^{87}Rb. The fraction trapped is measured by quick (2 ms) recapture into a magneto-optical trap (MOT) and comparing the fluorescence signal to that of the full MOT signal. Elastic collisions with the background gas result in an exponential decay allowing us to fit to this model and extract the loss rate.

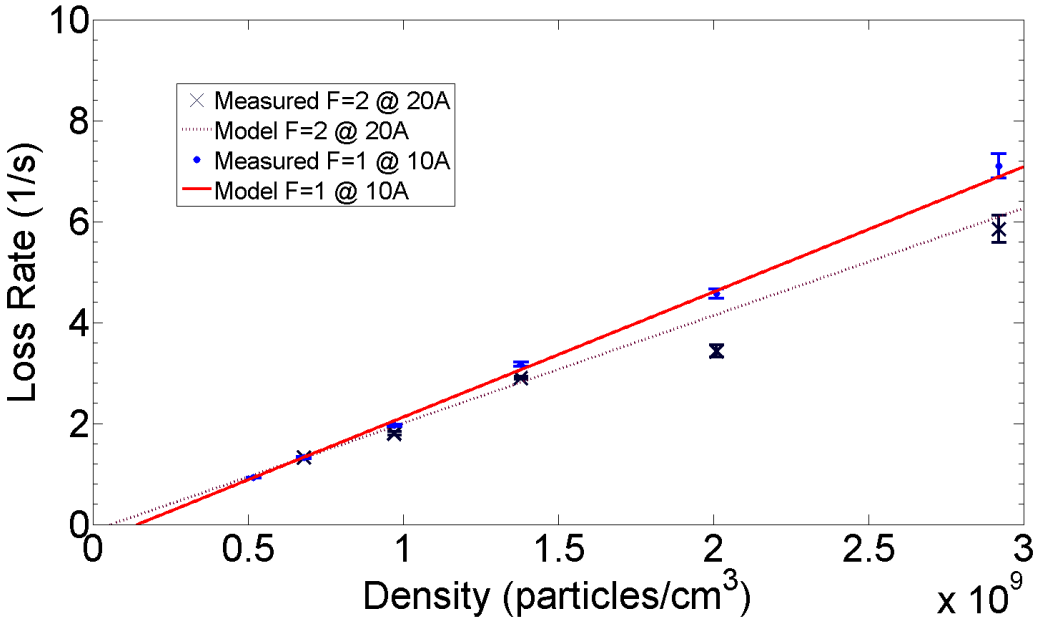

Figure 5.4: The loss rate in the magnetic trap is plotted over varying background density, where increased background density results in more elastic collisions, and hence increased loss rate. The sample plot shown is for a magnetic trap loaded with ^{87}Rb with increasing background argon density. The cross section can then be extracted from a linear fit to the loss rate.

while the trapped atoms undergo elastic collisions, and then turning the lasers back on (with MOT current levels) in order to measure the remaining fluorescence signal. This is then compared with the full MOT signal and background flurosence level to calculate $f(t)$ as the ratio of remaining signal to total MOT signal. In order to measure the remaining signal in the magnetic trap we need to average over about 50ms in time. This causes a problem, the atoms may begin loading into the MOT and as a result cause an increase in the measured signal. To correct this, we use a linear fit (not a simple average) and account for the expected increase in signal over the time interval the measurements are taken.

As with the MOT, we then repeat these measurements over a range of background gas densities and plot the loss rate as a function of gas density, as shown in Fig. 5.4 which shows sample results for $^{87}\mathrm{Rb} - Ar$. As you can see in Fig. 5.4, we are able to trap a specific F-level ground state by using optical pumping during the magnetic trap loading process. By varying the current in the magnetic trap, we can change the trap depth as estimated by Eq. 2.72; this will allow for

Trap Type	Trap Parameters	Loss Rate Slope Γ / n_a (cm^3/s)	Cross Section $\frac{\Gamma}{n_a<v_a>}(\mathring{A}^2)$
MOT	12 MHz detuning	5.23(3)x 10^{-10}	132(1)
MT	$\|F = 1 >$ @ 10A	2.48(3) x 10^{-9}	628(8)
	$\|F = 1 >$ @ 20A	2.26(1) x 10^{-9}	572(3)
	$\|F = 2 >$ @ 20A	2.13(3) x 10^{-9}	539(8)
	$\|F = 2 >$ @ 6A	2.28(14) x 10^{-9}	577(35)

Table 5.1: Experimental measurements of the loss rate slope and estimated cross section are shown for trapped ^{87}Rb and background argon density for both the magnetic and magneto-optical trap. The variance in cross section over the different trapped hyperfine states and between trap types is predicted to be caused by the difference in trap depths.

comparison with our theoretical results.

5.3 Trap Comparison

Table 5.1 below shows the overview of results obtained from the experimetal process used in both trap types. The corresponding trap depths will be calculated and used in comparison with theoretical predictions in the discussion chapter to follow.

Chapter 6

Numerical Results

Here we will present numerical results of the various calculations, which will be discussed in detail in the next chapter.

6.1 Cross Section vs Trap Depth

These results are performed using the procedure outlined in Chapter 4, where the potential coefficients are $C_6 = 280$ (atomic units), and C_{12} is chosen to set the potential well depth to $50cm^{-1}$. This is the primary result of interest and is what will be compared with experimental results extracting from the loss rate. We investigate cross section dependance on trap depth both for the expected case ($< \sigma_{\text{loss}} >$) and the single speed case ($\sigma_{\text{loss}}(\mu|v_{\text{Bg}}|/\hbar)$). The expected case is integrated over the distribution, and is hence calculated as a weighted average of the single speed curves and we have shown examples of these in Fig. 6.1. As shown, there is a slight (¡ 10 %) difference between the cross section of the mean speed (at 295K) and the result from the weighted average. Extraordinarily, the data predicts a drop in the measured cross section by over a factor of 3 for trap depths approaching $1K$. Recall, the mean speed is given by v_{th} from Eq. 2.33. The total cross section in the limit of zero trap depth is 668.7 $\mathring{A}$.

6.2 Cross Section vs Collision Speed

It is interesting to look at the behaviour of the cross section across the Boltzmann distribution. By calculating the cross section (evaluated at a chosen trap depth) across the Boltzmann distribution, we can see the trend on collision speed v_{Bg}. In particular, we observe oscillatory behaviour at low collision speeds, which dampen as the relative collision speed increases. This is shown for several trap depths, and you can see that the measured cross section will be zero below a certain speed for a given (non-zero) trap depth.

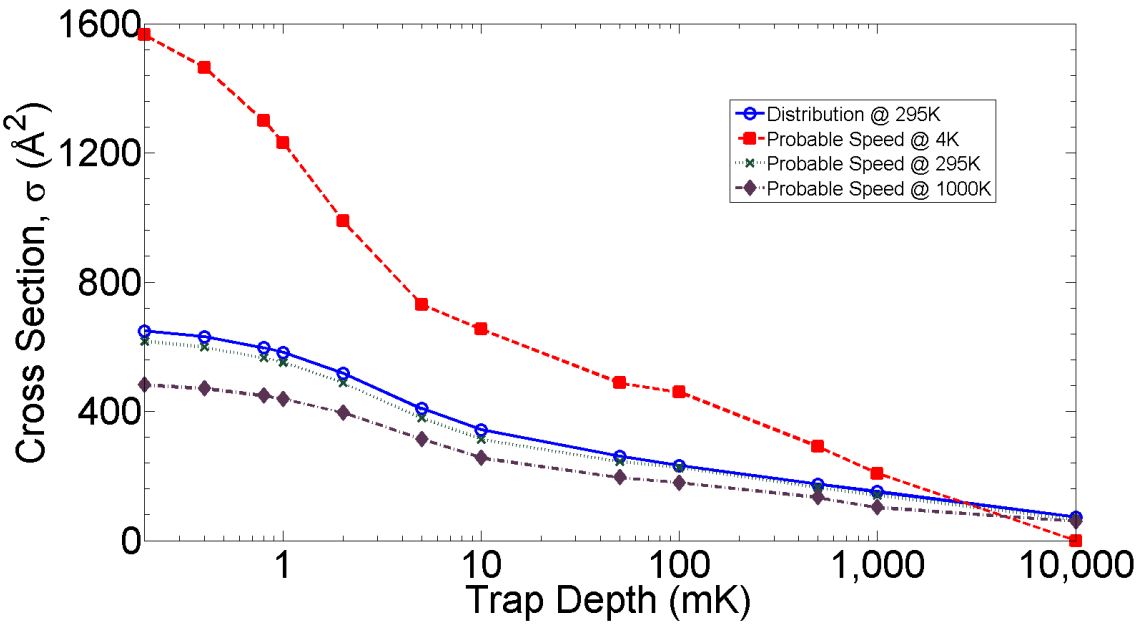

Figure 6.1: The theoretical cross section predictions as a function of trap depth are shown for trapped ^{87}Rb and background argon gas. The calculations are based on scattering theory, and a Leonard-Jones potential with C_6=280 (atomic units) and $C_12 = 50cm^{-1}$. Results are shown for cross sections integrated over the Maxwell-Boltzmann distribution as well as cross sections evaluated at the most probable speed of a given temperature.

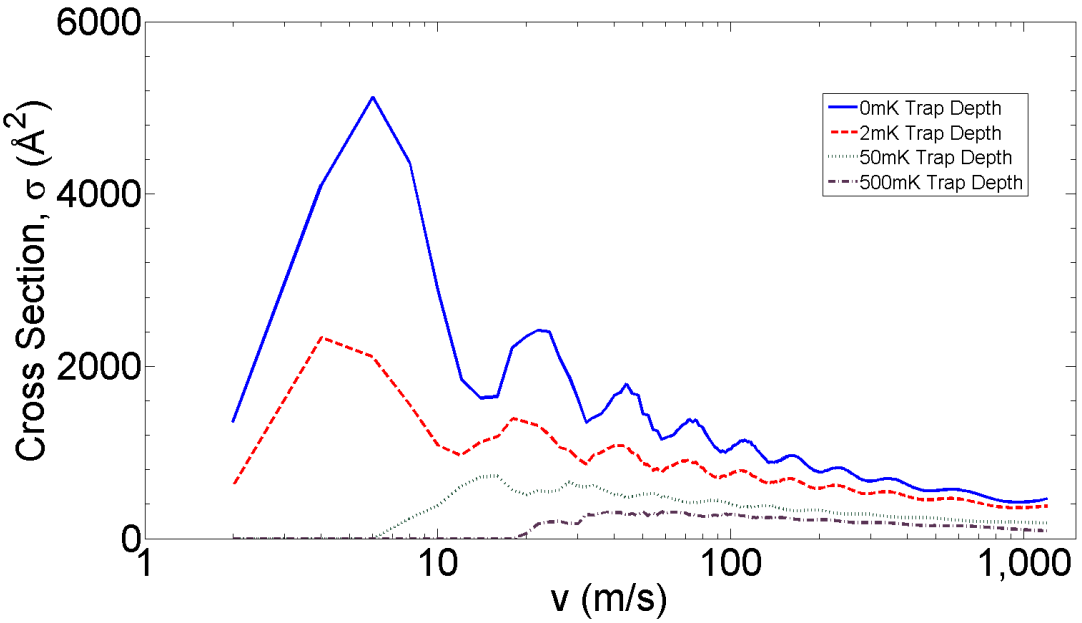

Figure 6.2: The theoretical cross section predictions as a function of relative collision speed are shown for various trap depths of trapped ^{87}Rb and background argon gas. The calculations are based on scattering theory, with a Leonard-Jones potential with C_6=280 (atomic units), $C_12 = 50cm^{-1}$, where the cross section is evaluated at the given speed.

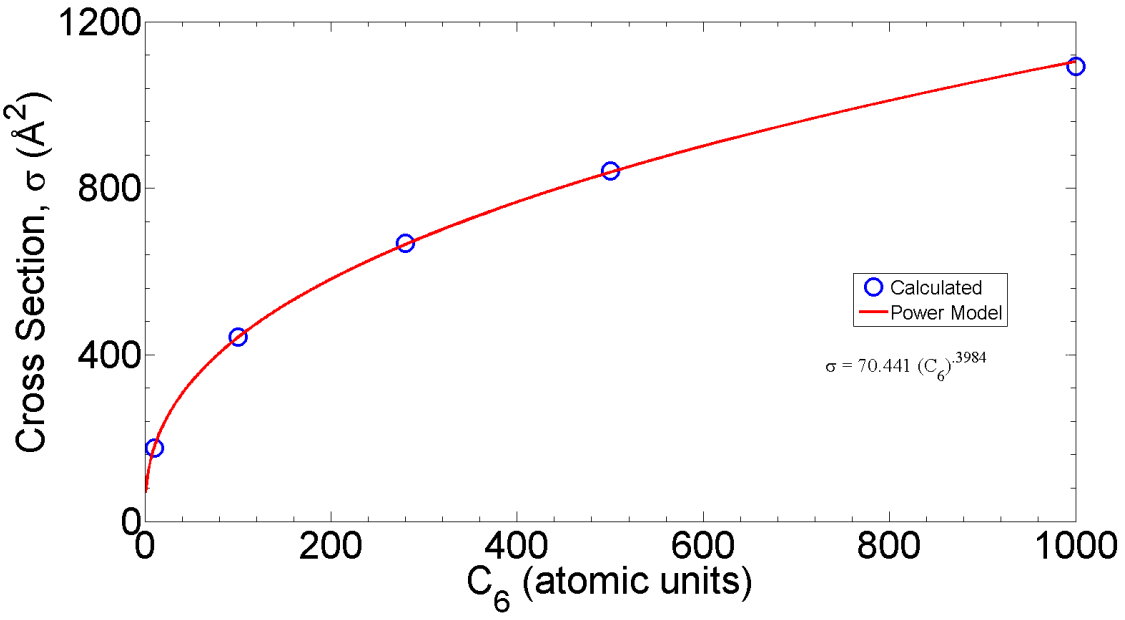

Figure 6.3: The theoretical cross section results are shown as a function of the Leonard-Jones potential C_6 coefficient. The calculations are based on scattering theory, and a Maxwell-Boltzmann distribution at 295K, and a C_{12} coefficient of $50cm^{-1}$. The cross section predictions are fit to a power law which shows good agreement with the expected power dependence of 2/5.

6.3 Cross Section vs C_6

Although theoretical predictions estimate the cross section approximately, our calculations converge to the exact solution, so it is useful to check how our solution compares to the analytical approximation. The cross section is studied for C_6 values over a wide range around the value previously cited for Argon. As shown in Fig. 6.3 we fit a power law which shows a very close relationship to the predicted model in Eq. 4.16.

6.4 Cross Section vs C_{12}

Given that the calculations for the cross section rely on matching long range asymptotic effects, we predict that the C_{12} value will not influence the resulting cross section, this prediction is confirmed by estimations made by Landau and Lifshitz [30]. From a numerical standpoint, however, C_{12} affects the convergence of a given integration range. As C_{12} increases, we need to integrate to

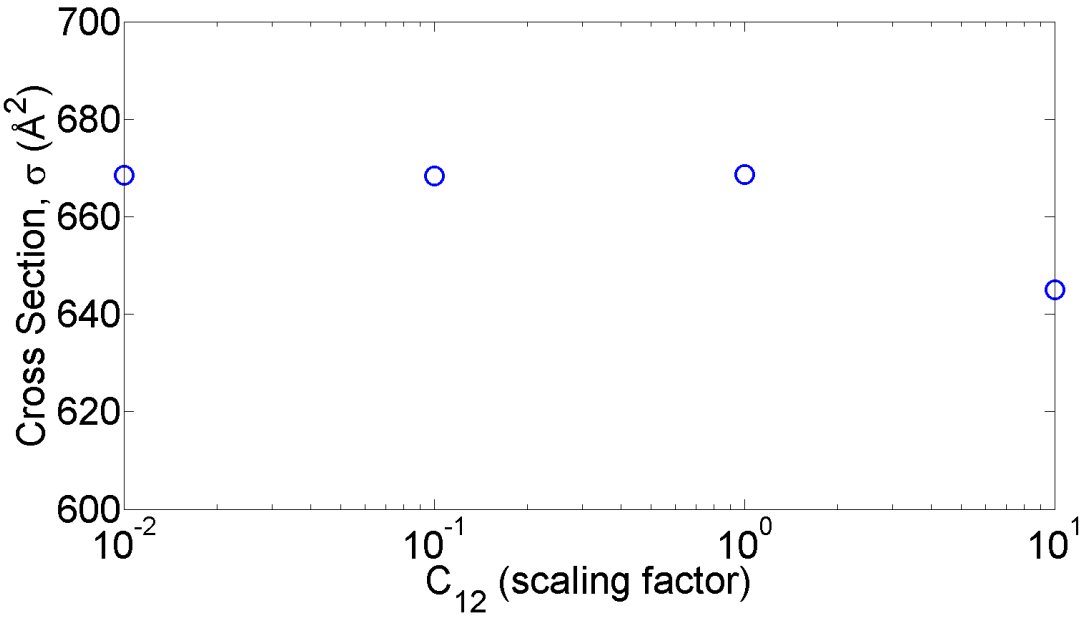

Figure 6.4: The theoretical cross section results are shown as a function of the Leonard-Jones potential C_12 coefficient where the values are normalized to $50cm^{-1}$. The calculations are based on scattering theory, and a Maxwell-Boltzmann distribution at 295K, and a C_6 coefficient of 280 (atomic units). As expected, the C_12 plays little role in the resulting cross section, remaining stable to within at least an order of magnitude.

further and further r in order to get a good estimate of the asymptotic behaviour. Similarly, as C_{12} decreases, we need to ensure we start the integration where the initial condition is valid. In Fig. 6.4, we show the dependence of the cross section on C_{12} when we ensure proper convergence is maintained. For this plot, the C_{12} values have been normalized to the standard value used (creating a potential well depth of $50cm^{-1}$).

6.5 Cross Section vs Collision Energy

As elastic cross sections are often cited in literature, it is important to recognize that the values obtained vary with collision energy. We study this relationship, calculating $< \sigma >$ for Maxwell-Boltzmann distributions centered around a range of temperatures (1K,10K, 100K, 295K, and 600K). Similar to the plot against C_6, the

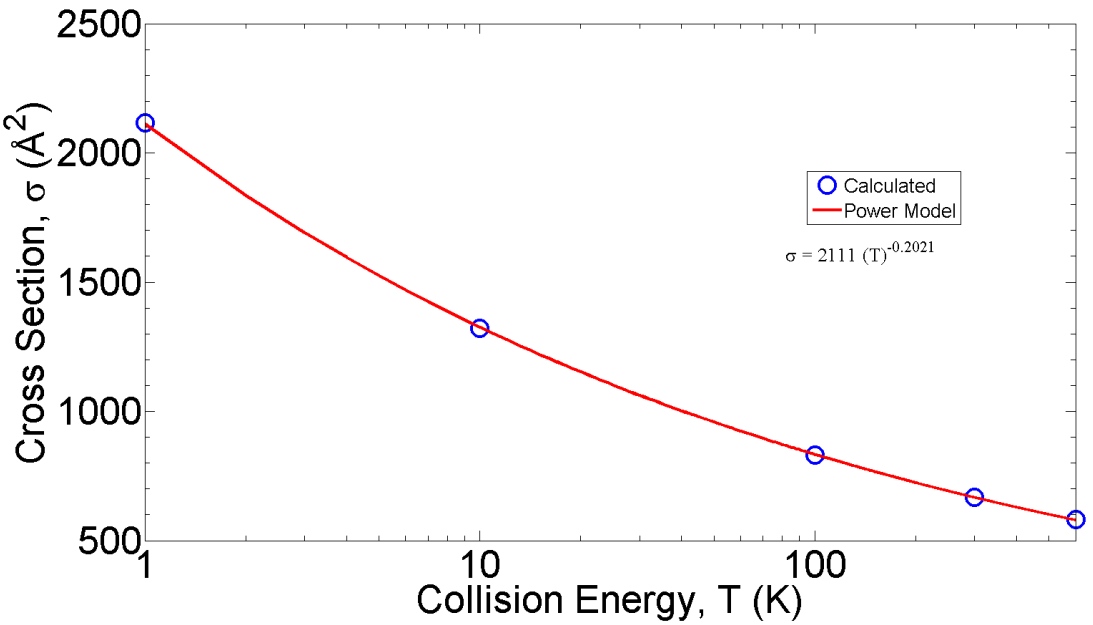

Figure 6.5: The theoretical cross sections are shown as a function of collision energy (T). The cross sections are calculated from scattering theory, and are integrated over the Maxwell-Boltzmann distribution centered at T. The results are fit to a power law, which shows good agreement to the predictions, and as expected, the cross section exhibits a power dependence of 1/5 on collision energy, corresponding to the traditional dependence on v of 2/5.

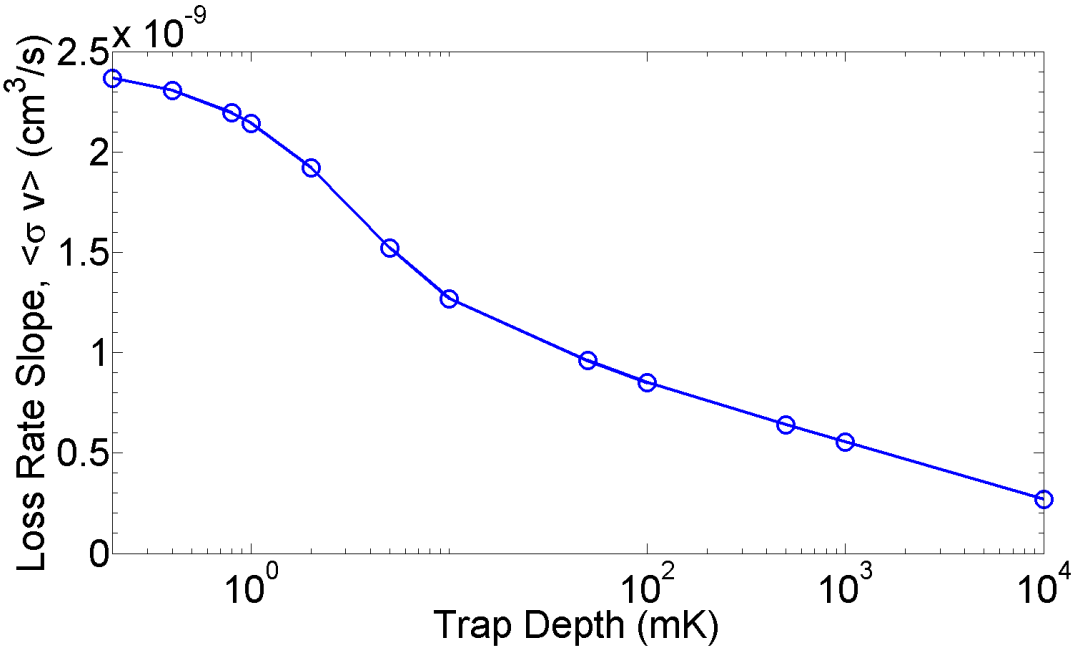

Figure 6.6: The expected loss rate proportionality constant for elastic collisions due to background gas of a given density is calculated as $< \sigma v >$ from scattering theory. These results are plotted against trap depth. The behaviour observed is similar to that of the expected collision cross section.

6.6 $< v\sigma >$ vs Trap Depth

As discussed earlier, the true comparison with experiment is better expressed as the expectation value, $< \sigma \vec{v}_{\mathrm{Bg}} >$. To do this we perform the same analysis, but with the corrected distribution weighting, and calculate the resulting proportionality constant of the loss rate, Γ which is linear in background gas density. This plot is shown against trap in Fig. 6.6 below and will be compared in the discussion section to follow.

Chapter 7

Discussion

7.1 Review of Past Work

This section will detail a few of the previous works related to elastic collision cross section measurements, including both theoretical and experimental studies.

7.1.1 Experimental Work

One of the earlier studies of collision cross sections by Rabi and Rosin[25], in 1935, used a molecular beam experiment in which a beam of atoms traversed a region of gas. From the reduction in outgoing intensity of the beam the mean free path and collision cross section are calculated. The experiment measures the outgoing intensity within a limiting angle of resolution, known as *scatteringangleresolution*. This resolution is analogous to our notion of trap depth and the total cross section is obtained in the limit of zero scattering angle resolution. There results include cross sections of both $Rb - Ar$ and $Rb - He$, which we can use for comparison to our results. Based on the same principles, the more recent experiment by Rothe and Neynbauer[26] suggests that previous experiments suffered from a pumping error with the McLeod gauge which may inflate cross sections by up to 30%. This paper also discusses the predicted relationship presented in Eq. 4.16 and quotes experimental C_6 values for various species combinations.

A paper published less than a year ago, by Matherson *et.al*[11] discusses a recent study similar to ours which investigates elastic collision cross sections with a metastable neon magneto-optical trap. In this work, it is claimed that the technique of using the MOT as a measurement tool, is capable of producing benchmark collision cross sections with significantly smaller error than past molecular beam experiments. It should be noted here that the Matherson paper brushes off a serious investigation of trap depths and makes a simple claim that given their estimated trap depths, they are measuring within uncertainty of the total cross section (zero trap depth). Upon applying the theoretical framework described in this thesis with the corresponding capture

velocities from Matherson *et.al* and their cited C_6 coefficient for the Leonard-Jones potential, the results estimated predict a significant difference between the measured and total cross sections. The results of their paper suggest a variance of cross section of about 15% over their range of detuning (and hence trap depth). However, as depicted in our theoretical predictions for the $^{87}\mathrm{Rb} - Ar$ MOT trap depth range of (1K) as shown in Fig. 6.1, it is possible to have this variance over a wide range of trap depth but still be well below zero trap depth limit. As a result, glancing collisions (that result in imparted energy < 1 K) are extremely important, and the trap depth should be well considered when using the MOT as a cross section measurement tool. Furthermore, this provides significant motivation to use the magnetic trap in order to measure collision cross sections in place of the MOT. The magnetic trap also has no source of zero light-assisted collisions, and ensures that the cross section is not a mixture of ground and excited state cross sections.

7.1.2 Theoretical Work

There has also been previous works which have calculated, from a theoretical standpoint, the C_6 value for our system of $^{87}\mathrm{Rb} - Ar$ (which was used for the theoretical analysis). In particular, the paper by Davison and Dalgarno [28] and another by Mahan [29] in the late 1960s discuss such a calculation. Mahan claims that the *analytical* formula for the C_6 coefficient presented in the work is equivalent to the calculation by Dalgarno and Davison. This calculation uses the excited relative energies of the gas electrons and matrix elements for their transitions. Overall, the theoretical works produce similar C_6 coefficients to the experimental works and this suggests that it is a reliable estimate for our Leonard-Jones potential.

The paper by Croucher and Clark in 1969[27] provides an excellent summary of the atomic molecular beam experiments as well as the theoretical papers discussed in this section.

7.1.3 Comparison to Rabi and Rosin

A comparison of our predicted cross sections is compared to the results of Rabi and Rosin in Table 7.1. Although not explicitly stated by their work, the collision energies are significantly higher in molecular-beam experiments and this can lead to a reduction in the measured cross section as predicted in Fig. 6.5. Overall, our results are in the range of previous results for $Rb - Ar$ and we find good agreement between theory and experiment.

Measured Cross Section ($\mathring{A}^2$)	Theoretical Cross Section ($\mathring{A}^2$)	Rabi and Rosin Cross Section ($\mathring{A}^2$)
628(8)	669	572

Table 7.1: The measured cross section of ^{87}Rb-Ar ($|F = 1>$ at 10A) is compared to that of the theoretical prediction (U_0=0) and to the result predicted by Rabi and Rosin. The cross section presented by Rabi and Rosin is expected to be reduced due to higher collision energy.

State	Current (A)	U_0^{axial} (mK)	U_0^{radial} (mK)
$\|F = 1, m_{\text{F}} = -1>$	10	0.084	0.30
	20	0.68	0.60
$\|F = 2, m_{\text{F}} = 2>$	6	0.20	0.36
	20	1.9	1.2

Table 7.2: The prediction of magnetic trap depths for the given (pure) spin states in both radial and axial directions are shown for ^{87}Rb. The estimates are based on the numerical estimate of the gradient from the magnetic coils.

7.2 Theory and Experiment

7.2.1 Trap Depths

In order to compare our experimental results with the theoretical, we first calculate the magnetic trap depths. The results for the magnetic trap depths of the various trapping states and currents are shown below in Table 7.2 where we have used Eq. 2.72 and Eq. 2.73 as the estimates. It is assumed at each F-level, that the spin mixtures are pure. This is exact for the $|F = 1>$ hyperfine state, but could be a mixture for the $|F = 2>$ state. At a current of 6A however, it is estimated that our gradient is not sufficient to trap the $|F = 2, m_{\text{F}} = 1>$ state, which results in a pure state of $|F = 2, m_{\text{F}} = 2>$. At 20A, the spin mixture is unkown, but for comparison has been included under the same assumption that it is a pure spin mixture of the higher spin state m_{F}=2. Given this assumption, we assign the average of the radial and axial trap depths to the $< \sigma \vec{v}_{\text{Bg}} >$ magnetic trap data. An accurate estimation of the MOT trap depth is still underway, but citations of capture velocities producing trap depths on the order of 1K are common and this is what we will use for comparison to the theoretical predictions.

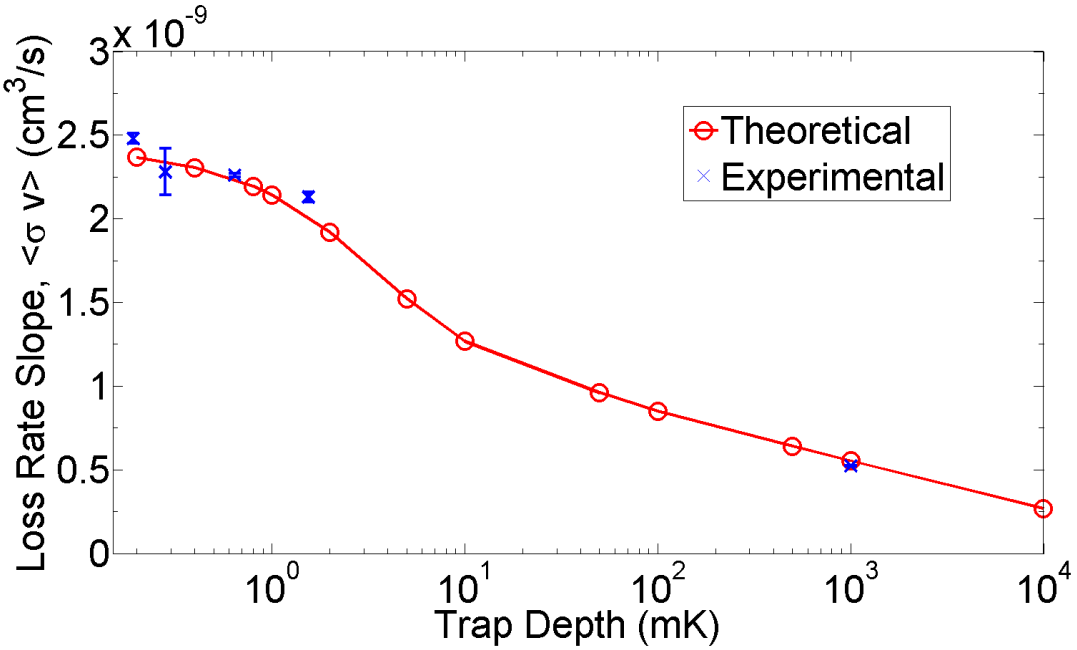

Figure 7.1: Theoretical predictions of $< \sigma \vec{v}_{\mathrm{Bg}} >$ for *Rb-Ar* are compared with experimental measurements. The sharp decline over the range of experimental trap depths is in good agreement with theoretical predictions. Magnetic trap depths presented are based on the average of theoretical estimates of the corresponding radial and axial trap depths. The magneto-optical trap depth is a rough estimate based on cited capture velocities.

7.2.2 Comparison

The comparison of $< \sigma \vec{v}_{\mathrm{Bg}} >$ is shown in Fig. 7.1, where you can see excellent agreement with theoretical predictions. Although the data may not always lie within errorbars, the main result is the rapid decline in the measured loss rate as the trap depth approaches 1K (MOT range). It is believed that this is the first investigation into cross sections and loss rates against trap depth, which compares both experimental and theoretical results. From a physical point of view it is astounding that recapture plays such a significant role over this range in trap depth implying that room temperature distributed particles imparting energies below 1K are the majority of the collision events.

7.3 Conclusions

Recently, the Magneto-Optical trap has been proposed as a capable tool of producing benchmark collision cross sections.[21] It is shown in this work that although the MOT may be capable, it is important to consider the trap depth associated with a given trap and to determine if it is an accurate measurement of the total cross section. As a result, the magnetic trap (which has significantly less trap depth), may be a better alternative when available.

Bibliography

[1] M. H. Anderson, J. R. Ensher, M. R. Matthews, C. E. Wieman,and E. A. Cornell, 1995, Science 269, 198.

[2] R. Folman et al., Phys. Rev. Lett. 84, 4749 (2000).

[3] M. A. Cirone, A. Negretti, T. Calarco, P. Krger, and J.Schmiedmayer, Eur. Phys. J. D 35, p.165. (2005).

[4] F. J. d. Heer and M. Inokuti, Electron Impact Ionization (Springer, New York, 1985).

[5] E. W. McDaniel, Atomic Collisions (Wiley, New York, 1989).

[6] R. Rejoub, B. G. Lindsay, and R. F. Stebbings,Phys. Rev. A 65, 042713 (2002)

[7] Robert Celotta, Howard Brown, Robert Molof, and Benjamin Bederson Phys. Rev. A 3, 1622 - 1628 (1971)

[8] C. D. J. Sinclair, E. A. Curtis, I. Llorente Garcia, J. A. Retter, B. V. Hall, S. Eriksson, B. E. Sauer, and E. A. Hinds, Phys. Rev. A 72, 031603(R) (2005)

[9] J. J. Tollett, C. C. Bradley, C. A. Sackett, and R. G. Hulet, Phys. Rev. A 51, R22 - R25 (1995)

[10] T. Calarco1,2, E. A. Hinds3, D. Jaksch1, J. Schmiedmayer4, J. I. Cirac1, and P. Zoller1, Phys. Rev. A 61, 022304 (2000)

[11] K. J. Matherson, R. D. Glover, D. E. Laban, and R. T. Sang, Rev. Sci. Instrum. 78, 073102 (2007).

[12] H. J. Metcalf and P. V. d. Straten, Laser Cooling and Trapping (Springer-Verlag, New York, 1999).

[13] T. P. Meyrath, Experiments with Bose-Einstein condensation in an optical box, Doctoral dissertation, The University of Texas at Austin.(2005)

[14] F. Reif, Fundamentals of Statistical and Thermal Physics (McGraw-Hill, New York, 1965).

[15] William D. Phillips,Rev. Mod. Phys. 70, 721 - 741 (1998)

[16] W. Demtroder, Laser Spectroscopy (Springer, New York, 1982), pp. 105-106.

[17] J. Weiner, V. S. Bagnato, S. Zillo, and P. S. Julienne, Rev. Mod. Phys. 71, 1 (1999).

[18] D. Jaksch, H.-J. Briegel, J. I. Cirac, C. W. Gardiner, and P.Zoller, Phys. Rev. Lett. 82, 1975 (1999).

[19] R.L. Garwin, L.M. Lederman, M. Weinrich, Phys. Rev. 105, (1957) 1415.

[20] *Muon Science* edited by S.L. Lee, S.H. Kilcoyne, and R. Cywwinski, published by SUSSP publications and the Institute of Physics U.K. (1999).

[21] K. J. Matherson, R. D. Glover, D. E. Laban and R. T. Sang, Physical Review A 78, 042712 (2008).

[22] Keith Ladouceur B. Experimental advances towards a compact dual-species laser cooling apparatus. Master's thesis, UBC.

[23] D.J. Griffiths. Introduction to Quantum Mechanics. Prentice Hall, 2005.

[24] D.J. Griffiths. Introduction to Electrodynamics. Prentice Hall, 2007.

[25] S. Rosin and I. I. Rabi, Phys. Rev. 48, 373–379 (1935).

[26] E. W. Rothe and R. H. Neynaber, Jour. Chem. Phys. 42, 3306-3309 (1965).

[27] D. J. Croucher and J. L. Clark, Jou. Phys. B. 2, 603-623 (1969).

[28] A. Dalgarno and W. D. Davison, Mol. Phys. 13, 479 (1967).

[29] G. D. Mahan, J. Chem. Phys. 48, 950 (1968)

[30] L. D. Landau and E. M. Lifshitz, Quantum mechanics, non-relativistic theory. (1958).

[31] W. H. Press, S. A. Teukolsky, W. T. Vetterling, and B. P. Flannery, Numerical Recipes in C++. Cambridge University Press 2002.

[32] N. Markovic, Notes on Scattering Theory (unpublished) (2003).

[33] F. Reif, Fundamentals of Statistical and Thermal Physics (1965).